8-5-2006

Finite Element-Boundary Integral Method And Its Application To Implantable Antenna Design For Wireless Data Telemetry

Jose S. Pvillalta

Recommended Citation

Pvillalta, Jose S., "Finite Element-Boundary Integral Method And Its Application To Implantable Antenna Design For Wireless Data Telemetry" (2006). *Theses and Dissertations*. 2292.
https://scholarsjunction.msstate.edu/td/2292

FINITE ELEMENT-BOUNDARY INTEGRAL METHOD AND ITS APPLICATION TO IMPLANTABLE ANTENNA DESIGN FOR WIRELESS DATA TELEMETRY

By

Jose S. Pvillalta

A Thesis
Submitted to the Faculty of
Mississippi State University
in Partial Fulfillment of the Requirements
for the Degree of Master of Science
in Electrical Engineering
in the Department of Electrical and Computer Engineering

Mississippi State, Mississippi

August 2006

FINITE ELEMENT-BOUNDARY INTEGRAL METHOD AND ITS APPLICATION TO IMPLANTABLE ANTENNA DESIGN FOR WIRELESS DATA TELEMETRY

By

Jose S. Pvillalta

Approved:

Erdem Topsakal
Assistant Professor of Electrical and
Computer Engineering
(Director of Thesis)

Nicholas H. Younan
Professor and Graduate Program Director
of Electrical and Computer Engineering

John Patrick Donohoe
Professor of Electrical and Computer
Engineering
(Committee Member)

Hyeona Lim
Assistant Professor of Mathematics and
Statistics
(Committee Member)

Dr. Roger L. King
Associate Dean for Research and Graduate Studies

Name: Jose S. Pvillalta

Date of Degree: August 5, 2006

Institution: Mississippi State University

Major Field: Electrical and Computer Engineering

Major Professor: Dr. Erdem Topsakal

Title of Study: FINITE ELEMENT-BOUNDARY INTEGRAL METHOD AND ITS
APPLICATION TO IMPLANTABLE ANTENNA DESIGN FOR
WIRELESS DATA TELEMETRY

Pages in Study: 69

Candidate for Degree of Master and Science

A non-stationary Krylov subspace based iterative solver for the three dimensional finite element-boundary integral (FE-BI) method for implantable antennas is presented. The present method numerically solves the frequency domain Maxwell's equations in the variational form to formulate the finite element solution using hexahedral discretization elements in conjunction with the appropriate boundary integral equations. Four different solvers are used to investigate the convergence behavior of the FE-BI technique on the design of the antennas. The scheme is then applied to two miniaturized planar inverted-F antennas (PIFA): a serpentine and a spiral. The antennas are designed for the Medical Implant Communication Service (MICS) band (402-405 MHz). Validations and comparisons are done using High Frequency Electromagnetic Simulation (HFSS) software. Return loss, gain, near fields, and far fields are presented for the serpentine and spiral antenna.

DEDICATION

I would like to dedicate this thesis to my mom, Rosa C. Chavez, who has been a great source of motivation, and inspiration that helped me achieve all that I have achieved.

ACKNOWLEDGEMENTS

I would like to express my appreciation to the many people without whose selfless assistance this thesis could not have materialized.

First and foremost, I would like to extend my deepest gratitude and thanks to my advisor, Dr. Erdem Topsakal, for all his time, help, constant support, guidance, and understanding in the development and completion of this thesis.

I would like to thank Dr. J. Patrick Donohoe and Dr. Hyeona Lim for their valuable time for serving on my committee.

Finally, I would also like to give my sincere thanks to my fellow colleagues, Tutku Karaçolak and A. Zachary Hood for sharing their knowledge and experience with me selflessly during our time spent together working on this thesis.

TABLE OF CONTENTS

CHAPTER Page

LIST OF TABLES

LIST OF FIGURES

FIGURE Page

CHAPTER I

INTRODUCTION

1.1 Overview

Wireless technology for implantable antennas has been increasingly researched for medical applications. The benefits of this application, such as in medical telemetry for example, can be used to monitor a patient's physiological vitals over a distance via radio-frequency (RF) technology. As designers develop new implanted medical devices taking advantage of RF technology to improve the quality of care for patients, antennas are key to these new systems (see Figure 1.1 and 1.2).

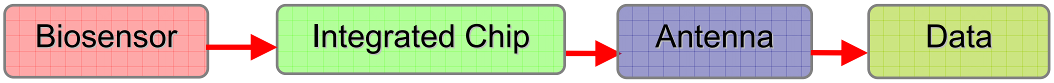

Figure 1.1

Block diagram of system process

An in-human wireless medical system (implantable device) brings up some rigorous challenges. Some of the issues involved with in-body systems are: heating of the surrounding tissue, compatibility of materials with the body's physiology, and the power consumption needed to operate the implantable device. An implantable antenna must satisfy stringent size and weight constraints while simultaneously achieving over the proper band and radiating characteristics. The design must radiate outside the body effectivily and efficiently while complying with the radiation requirements of the power associated to drive the device.

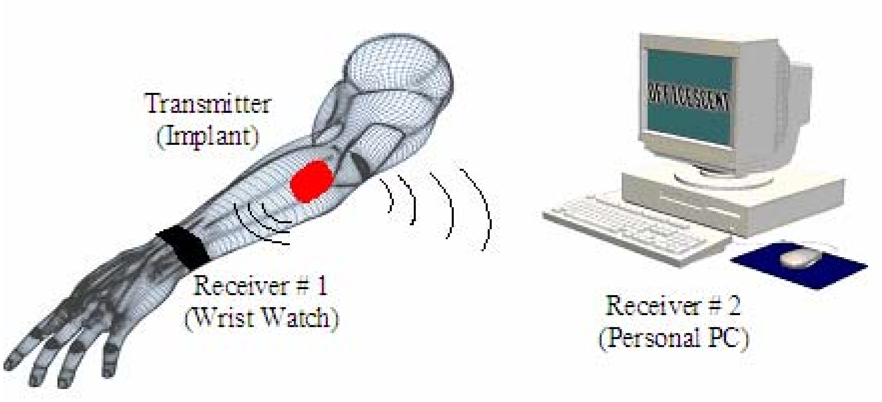

Figure 1.2

Wireless data telemetry system

Numerical simulation tools that are fast and accurate are crucial in developing reliable and efficient implantable antenna systems. The most common technique used to evaluate these systems is the finite-difference time-domain (FDTD) method. The non-stationary Krylov subspace-based iterative solvers for the FE-BI simulation of implantable antennas are investigated. Solvers play an important role in the convergence characteristics, and primarily determine the total solution time for a given problem. Therefore, it is very crucial to investigate and understand the convergence behaviour of these solvers.

1.2 Organization of Thesis

This thesis is organized in the following manner. Chapter 1 contains a brief foreword about the project. The motivation of the task is well defined with the problematic obstacles that must be overcome. The differences between the FDTD and FE-BI algorithm approaches when solving electromagnetic problems of implantable antennas are also introduced. Chapter 2 begins with an introduction to electromagnetics and the different types of fields engaged in the discipline with relevant examples. The communication method that needs to be accounted for when designing an implantable antenna is overviewed. A brief discussion on the characteristics of the parameters of the material(s) (mediums) involved is also introduced. Antenna information for similar procedures is reviewed as well. The chapter closes with numerous references to previous work related to the primary thrust of the project, implantable antennas in the human body. Chapter 3 begins with an introduction to the governing Maxwell's equations with the solution to the electric field for lossy medium in a homogenous space. The properties of a lossy medium are then stated in order to design proper antennas. A detailed three dimensional numerical formulation based on the frequency domain is presented for the FE-BI method, with its discretization domain also included in this chapter. An iterative method is defined with a list of non-stationary Krylov subspace-based iterative solvers that are commonly used to solve linear matrix systems are discussed in Chapter 4. A brief mathematical descriptive background of Krylov subspace methods is also introduced. Chapter 4 also contains a brief explanation of the applications and properties of preconditioners. Chapter 5 covers the applications of the techniques explained in Chapters 3 and 4. Detailed numerical results are also given for the antennas characteristics in this chapter. In addition, comparisons regarding FE-BI with HFSS, are also reviewed. Concluding remarks and discussion of the potential of the present applications in future research are made in Chapter 6.

CHAPTER II

BACKGROUND AND PREVIOUS WORK

2.1 Introduction

The use of electromagnetic (EM) waves has numerous of benefits in our daily lives such as mobile phones, radar detection devices, microwave ovens, and medical diagnostic tools. However, with any new technology comes the potential for unwanted side effects. Some applications of electromagnetic waves are so new that researchers have been unable to study all possible impacts. The exploration of the potential uses of electromagnetic fields, as well as characterizing their possible negative side effects, must be researched extensively when dealing with medical applications. All electromagnetic phenomena are governed by Maxwell's equations. Radio frequency (RF) technology is one form of electromagnetic energy that has been used for a variety of medical applications and research (i.e. Magnetic Resonance Imaging (MRI), Computerized Axial Tomography (CAT) Scan, hyperthermia treatment for cancer, etc.). RF energy delivery has become the dominant modality of medical research.

To this day, Maxwell's equations remain the fundamental laws that drive engineering to design, evaluate, and characterize electromagnetic phenomena concerning antennas. The equations have a strong predictive power that is very important in many engineering and scientific disciplines in EM analysis (see Figure 2.1). A complete solution of Maxwell's equations can expedite many design and analysis processes. In the past, EM analysis has been traditionally performed with either simple geometry, or approximate pencil-and-paper (analytical) methods. Nowadays, with the help of computers and computer-aided software, the solutions of large, complex EM problems are now achievable.

As computer technology advances on its computational potential, Computational Electromagnetics (CEM) is becoming a more actively researched disciplinary field. This field engages various numerical methods involving iterative solvers, solving complex EM problems through Maxwell's equations. These numerical techniques are generally solved either by their partial differential equations (PDE), integral equations (IE), or a combination of both in conjunction with an iterative solver. The CEM tools provide a significant role in helping comprehend the general characteristics and physics of various electromagnetic field problems and their applications.

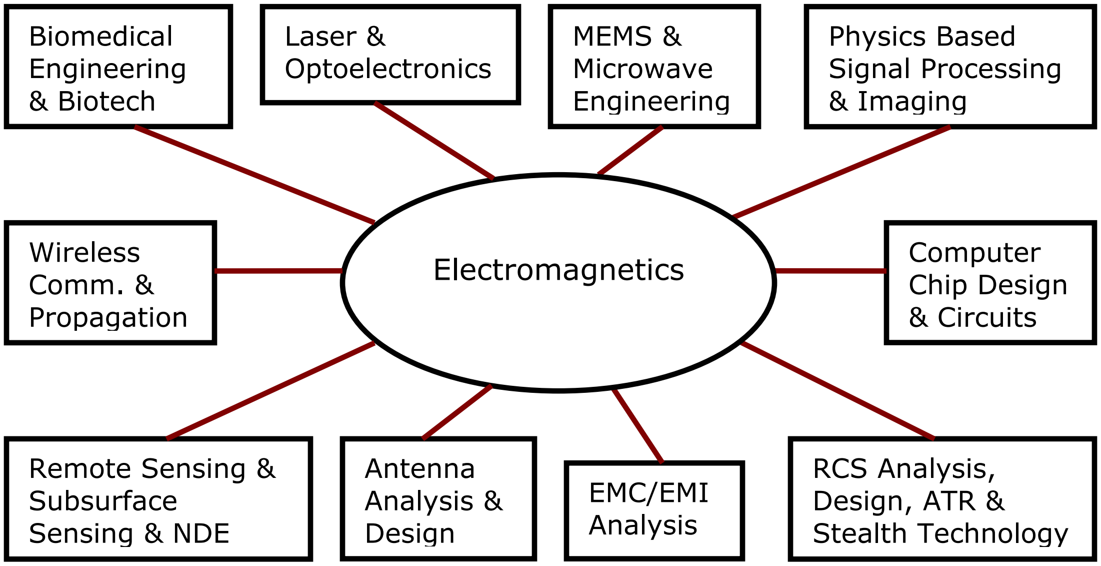

Figure 2.1

Illustration of various areas and discipline in EM

The primary interest in this thesis is the design and evaluation of low-profile implantable antennas using the FE-BI numerical technique in conjunction with non-stationary Krylov subspace based iterative solvers.

2.2 Communication Methods

With the increased use of medical implants, the growing need for flexible communication link between the implant and receiver outside the body must be analyze. To this day, the only form of communication between any implant and the outside world is done by an inductive link between the implant and an external coil at a low carrier frequency. The two coils are inductively coupled to each other since they are collinear, where the inductive coupling serves as the communication channel. For example, the range of communication (as in retrieving information from a heart pacemaker) is restricted to “touch” range, since the external coil housing must touch the patient’s chest. This procedure is time consuming, since the placement of the external coil, which is guided by an indicator, is sensitive to the position of the internal coil. For cardiac telemetry, dipole [1] and microstrip [12] patch antennas have also been considered.

Extended range and communication speeds are achieved by using a higher carrier frequency with a broader bandwidth. One frequency band applicable to this procedure is the newly standardized Medical Implant Communications Service (MICS) band, which has the benefit of being reserved mainly for medical and metrological applications. The European Telecommunications Standards Institute (ETSI) [2] standardized the MICS band [3]. The ETSI document lists two principal fields of application for the standard. The first application is concerned with the telecommunication between a base station and an implant device, and the second details the telecommunication of the medical implant within the same body. The frequency band allocated for the MICS band is 402 MHz to 405 MHz, and the maximum emission bandwidth that can be occupied is 300 kHz. The MICS band has two major advantages over the “touch” range lower frequency used as in heart pacemakers: the first is an increase in bandwidth, and the second is that the higher frequency gives rise to a propagating electromagnetic wave, which makes the system usable at a longer range.

The MICS frequency band is already in use by the Meteorological Aids Service (METAIDS), which is primarily used by weather balloons transmitting data back to the ground (earth). For this reason, the MICS system is specified only to be used indoors.

Another possible applicable band is the Industrial, Scientific and Medical (ISM) band, having an allocation of between 2.4000 GHz to 2.4835 GHZ. The major drawback here is that it is being heavily used by other applications, such as WiFi, Bluetooth, microwave ovens, cordless telephones, etc.

2.3 Characteristic of Tissue Parameters

The absorption of electromagnetic power within biological tissue is determined by the "tissue parameters". The primary influences are: relative permittivity (ε_r), electrical conductivity (σ), mass density (ρ), and relative permeability (μ_r), which is unity in a biological entity ($\mu_r = 1.0$). All the parameters mentioned above are dependent on the tissue temperature, and frequency. Bone, fat, cartilage, etc. have low conductivity while muscle, blood, brain, etc. have large conductivity values due to being water-based tissues. Since the conductivity and the relative permittivity in the tissue depend on the frequency used, ε_r is large and σ is small for lower frequencies and ε_r is small and σ is large for higher frequencies. The impedance, current, and attenuation values of living tissue vary with the frequency of the applied signal, and are strongly dependent on its dielectric permittivity and conductivity.

2.4 Antenna Design

Antenna design is a mature science today, and an engineering discipline with a large number of design manuals available [4]-[6]. All of these texts primarily describe antennas placed in a non-conducting environment with a constant relative permittivity of 1, or close to 1, and are antennas primarily placed in air. The closest embedded structure in use at this point is an antenna placed in a radome, which is made of low loss materials with low permittivity. Placing the antenna inside the body adds significant complexity to the design. The antenna is now surrounded by a lossy medium with a very high permittivity.

When an antenna is implanted in a lossy and finite body, as in a biological entity, the standard antenna theory, characteristics, and functions must be reevaluated in order to adjust the specifications utilized in the antenna design. The influence of the implant on the antenna's characteristics must also be considered. The analyses done must consider wave propagation from the antenna through the body into the air and over to a receiver. The complications of an implantable antenna are that it has to account for body shape and the actual placement of the implant. To add more complexity to the problem, the gain, directivity, and the efficiency will vary from one individual to another.

The antenna characteristics and performance will be altered when the antenna is attached to an object. If the antenna is also encased in order to protect it from the environment, like biological tissues, the performance of the antenna will be jeopardized even further. For these reasons, designing an implantable antenna that is efficient will require analysis of the characteristics, which will play an important role in the simulating technique used. The body covering the implanted antenna has to be accounted for when evaluating the far field radiation characteristics of an antenna operating in the MICS band. At 403.5 MHz the wavelength, defined as $\lambda = c/f$ where c is the speed of light and f is the operational frequency, in air is 0.74 m and about 0.09 m, $\lambda' = \lambda/\sqrt{\varepsilon_r}$ where ε_r is the relative permittivity of skin, skin deep in the body. Thus, the design and implementation of the antenna cannot be discussed or evaluated without investigating the electromagnetic properties of human tissues, which will influence the characteristics of the antenna.

2.5 Previous Work

Today there are many implants in use and in development. Some would benefit from an RF link. Some examples of these implants are: artificial eyes, muscle stimulators, cochlea implants, brain pacemakers for Parkinson's disease [9], implantable drug pumps [10], nerve signal recorders for use with robotic prostheses [11], heart pacemakers, etc. All of these implants need some kind of communication link between the devices and outside the body, either one way or in both directions.

High frequency antennas pertaining to medical implants are rare in the literature. A few well-reported designs and applications are shown [12]-[16], and some patents have been granted [16]-[18]. There are more published articles in the biomedical telemetry application, but they are primarily dealing with low frequency and utilize inductive coupling [19]-[22]. The systems are described both in the texts [23], [24] and in published articles. As stated previously, these systems primarily use coil antennas, which are one of the mostly commercially available implanted systems from Advance Telemetry Systems [25], as they use low frequencies for transmission.

Embedded microstrip antennas have also been used for several sensory applications, including sensors for dielectric property measurement [26], [27], detecting the presence of a dielectric object [28], moisture measurement [29], and geophysical well logging [30]-[32]. Embedded microstrip antennas have been used therapeutically for a number of applications, including cardiac ablation [33], [34], balloon angioplasty [35], and cancer treatment using hyperthermia [35]-[39].

2.6 Numerical Techniques

Numerical techniques have been used to solve and analyze numerous real-life complex EM problems using accurate mathematical models. These models are based on Maxwell's equations, which govern the EM phenomena, with their proper boundary conditions, using different numerical algorithms such as finite difference-time/frequency domain (FDTD/FDFD), finite element (FE) method, method of moments (MoM), and finite element-boundary integral method (FEBI). These methodologies can be classified broadly as frequency- and time-domain methods. Each of these two cases can also be subdivided into more specialized categories such as integral and differential methods, or spectral and spatial methods. In this thesis, the FE-BI technique will be employed to analyze the characteristics of the implantable antennas, since the technique computes complex three-dimensional geometries with arbitrary shapes in inhomogeneous media with ease.

CHAPTER III

GOVERNING EQUATIONS AND FORMULATIONS

3.1 Maxwell's Equations

Maxwell's equations are the fundamental law and basis for antenna design and wave propagation. The equations have a strong predictive power that is very important in analyzing and understanding the characteristics of antennas. Complete solution of Maxwell's equations can expedite many design and analysis processes. The following are the frequency domain Maxwell's equations:

$$\nabla \times \vec{H} = \vec{J} + \vec{J}_S + j\varpi\vec{D} \tag{3.1}$$

$$\nabla \times \vec{E} = -j\varpi\vec{B} - \vec{M} \tag{3.2}$$

$$\nabla \bullet \vec{D} = \rho_v \tag{3.3}$$

$$\nabla \bullet \vec{B} = 0 \tag{3.4}$$

where $\vec{D}$ is the electric flux density, $\vec{E}$ is the electric field, $\vec{B}$ is the magnetic flux density, $\vec{H}$ is the magnetic field, ρ_v is the charge density, ϖ is the angular frequency, $\vec{J}$ is the electric current density, and $\vec{M}$ is the magnetic current density. $\vec{J}_S$ is the added source current density on the antenna. Since linear isotropic materials are considered for most applications, the constitutive equations are:

$$\vec{D} = \varepsilon\vec{E} \tag{3.5}$$

$$\vec{H} = \frac{\vec{B}}{\mu} \tag{3.6}$$

$$\vec{J} = \sigma\vec{E} \tag{3.7}$$

where ε is the permittivity, μ is the permeability, and σ is the conductivity, which in general, are complex and frequency-dependent in lossy material.

In an infinite homogenous space, the electric field at radius *r* from an antenna can be obtained by solving Maxwell's equation for $\vec{E}(\vec{r})$ [40]:

$$\vec{E}(\vec{r}) = -j\varpi\mu\left(\bar{I} + \frac{1}{k^2}\nabla\nabla\right)\cdot\iiint_V \frac{e^{-jk\left|\vec{r}-\vec{r}'\right|}}{4\pi\left|\vec{r}-\vec{r}'\right|}\vec{J}_S(\vec{r}')dv' \tag{3.8}$$

where $\bar{I}$ is the identity operator, i.e., $\bar{I}\cdot\vec{J} = \vec{J}$. In addition, *V* is the volume containing the antenna, *r* is the distance from the antenna, and k is the complex wavenumber, defined as $k = \varpi\sqrt{\mu\varepsilon_c}$.

This formula is useful if the currents in a volume *V* are known, and are as stated above for homogenous space. The solution is also applicable even if the medium is lossy, i.e., for complex wavenumbers *k*, permittivity ε, permeability μ, and conductivity σ. In real life, and in most cases of electromagnetic problems, the current values are not known, and are usually composed of or in an inhomogeneous medium. Thus a numerical method must be employed in order to calculate the proper electric/magnetic fields with the suitable boundary conditions. For this reason the FE-BI method is engaged and explained in detail section 3.3.

3.2 Properties of Lossy Medium

In order to design an effective and efficient implantable antenna, the electromagnetic properties of the materials (human tissues) must be defined. When placing a radiating structure in a material with high permittivity, and with non-zero conductivity, the traditional antenna theory must be reviewed in order to modify the usual specifications used in antenna design.

The permittivity and conductivity in the general case are complex quantities that are expressed in their real and imaginary parts defined as:

$$\varepsilon = \varepsilon' - j\varepsilon'' \tag{3.9}$$

$$\sigma = \sigma' - j\sigma'' \tag{3.10}$$

and the complex permittivity ε_c of an arbitrary medium is then defined as:

$$\varepsilon_c = \varepsilon_e - j\frac{\sigma_e}{\varpi} \tag{3.11}$$

Here ε_e and σ_e are the effective permittivity and effective conductivity, respectively. They are defined as:

$$\varepsilon_e = \varepsilon' - \frac{\sigma''}{\varpi} \tag{3.12}$$

$$\sigma_e = \sigma' + \omega\varepsilon'' \tag{3.13}$$

The permittivity ε_e is often scaled as:

$$\varepsilon_r = \frac{\varepsilon_e}{\varepsilon_0} \tag{3.14}$$

where $\varepsilon_0 = 8.854 \times 10^{-12}$, which is the permittivity of vacuum.

The loss due to conductivity in a medium is expressed as a “dissipation factor”, *Diss*, or the loss tangent “δ”. They are defined as:

$$Diss = \tan\delta = \frac{\mathrm{Im}[\varepsilon_c]}{\mathrm{Re}[\varepsilon_c]} = \frac{\sigma_e}{\omega\varepsilon_e} \tag{3.15}$$

where $\mathrm{Re}[\ ]$ and $\mathrm{Im}[\ ]$ denote the real and imaginary part, respectively.

3.3 FE-BI Formulation

The characteristics of an electromagnetic (scattering and/or radiation) problem with an arbitrarily-shaped structure using the FE-BI method must first introduce a fictitious surface ∂B to enclose the system, in which the problem gets divided into an interior and exterior region. Within ∂B, the interior area, the finite element technique is employed to compute the fields inside. The principle of the method is to replace an entire continuous domain with a number of sub-domains, in which the unknown function is represented by interpolation functions with unknown coefficients. Each region (sub-domain) is referred to as an “element” and the process of subdividing a domain into a finite number of elements is referred to as “discretization”. Elements are connected at specific points, called “nodes”, and the assembly process requires that the solution be continuous along common boundaries of adjacent elements. The discretization of the domain is the first, and perhaps the most important step in any finite-element analysis, because the manner in which the domain is discretized will affect computer storage requirements, the computation time, and the accuracy of the numerical results. Outside ∂B, exterior region, the fields are represented by the radiation of the outside source(s) and a set of equivalent electric and magnetic currents placed on ∂B, by applying the boundary integral equations (BIE). By modeling the system as shown in Figure 3.1, the decoupling of the fields' interior and exterior to ∂B is permitted, and will be coupled later by enforcing tangential field continuity on ∂B by the basis functions [41]. From this concept, a system of equations is produced and the structure of the standard FE-BI system is of the form:

$$\begin{bmatrix} E^{vv} & E^{vs} & 0 \\ E^{sv} & E^{ss} & B \\ 0 & \Omega & \Theta \end{bmatrix} \begin{Bmatrix} E^{i} \\ E^{s} \\ H^{s} \end{Bmatrix} = \begin{bmatrix} b^{i} \\ g^{s} \\ b^{s} \end{bmatrix}. \tag{3.16}$$

where $[E^{i}]$ is the electric field vector within the boundary problem V, $\{E^{s}\}$ and $\{H^{s}\}$ are the vectors containing the electric and magnetic fields, respectively, on the boundary ∂B, $[E^{vv}]$, $[E^{vs}]$, $[E^{sv}]$, $[E^{ss}]$ are sparse sub-matrices associated with the stored energy, $[B]$ is the sparse matrix related to the energy existing throughout the boundary, $[\Omega]$, and $[\Theta]$ are the BI operators that interact with the surface electric and magnetic currents with each other via the free-space Green's function. The $[E^{vv}]$ and $[E^{ss}]$ matrices are symmetric and $[E^{vs}] = [E^{sv}]^{T}$, where the T superscript signifies the transpose.

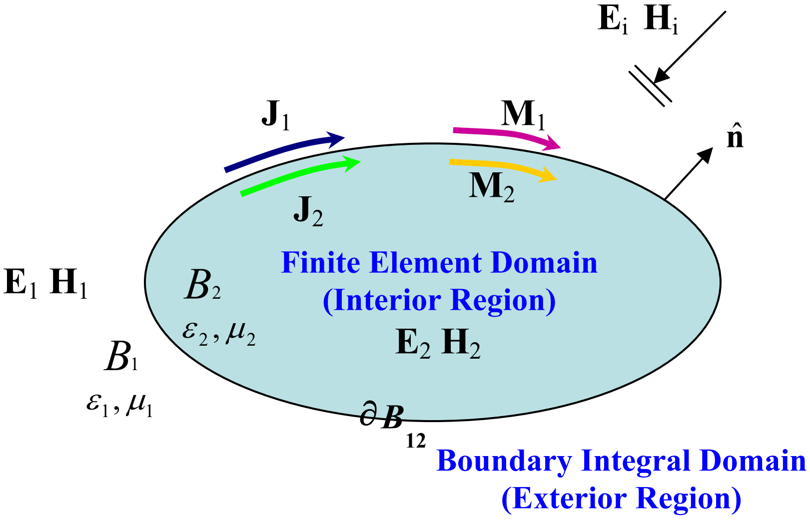

Figure 3.1

Finite Element and Boundary Integral Domains

3.3.1 Finite Element Formulation (Interior Region)

To formulate the fields inside the boundary ∂B, the functional $F(\vec{E})$ is derived by the generalized variational principle for vector problems. We first begin with the vector wave equation, which is given by:

$$\nabla \times \left(\frac{1}{\mu} \nabla \times \vec{E} \right) - k_0^2 \varepsilon_r \vec{E} = -jk_0 \eta_0 \vec{J}^{\text{int}} + \nabla \times \left(\frac{1}{\mu_r} \vec{M}^{\text{int}} \right) \tag{3.17}$$

where k_0 is the free-space wavenumber, defined as $k_0 = 2\pi/\lambda_0 = \omega\sqrt{\varepsilon_0 \mu_0}$, and η_0 being the free-space intrinsic impedance, define as $\eta_0 = \sqrt{\mu_0/\varepsilon_0}$.

A traditional approach for solving (3.17) is to consider the functional:

$$F(\vec{E})=\frac{1}{2}\iiint_V\left[\frac{1}{\mu_r}(\nabla\times\vec{E})\cdot(\nabla\times\vec{E})-k_0^2\varepsilon_r\vec{E}\cdot\vec{E}\right]dV+\iiint_V\vec{E}\cdot\left[jk_0\eta_0\vec{J}^{\,\text{int}}-\nabla\times\left(\frac{1}{\mu_r}\vec{M}^{\,\text{int}}\right)\right]dV$$
$$+\,j\eta_0k_0\int_S\vec{E}\cdot(\vec{H}\times\cdot\hat{n})\;dS \tag{3.18}$$

The fields in V can be formulated into the variational problem (shown above) by [42] with the presence of the second volume integral linking the internal electric and magnetic source $\left(\vec{J}^{\,\text{int}},\vec{M}^{\,\text{int}}\right)$ due to the antenna element feed(s). This can be shown to be stationary with respect to the solution of the vector wave equation shown above, with $\left(\vec{H}\times\hat{n}\right)$ being considered as one of the sources for $\vec{E}$. Thus $\vec{E}$ can be found by enforcing:

$$\partial F(\vec{E})=0 \tag{3.19}$$

where $\partial F(\vec{E})$ denotes the first-order variation of F about $\vec{E}$. To discretize the functional $F\left(\vec{E}\right)$, the volume V is subdivided into hexahedral volume elements which are explained in detail in the basis functions section.

Now that the interior region has been formulated from the finite element, the exterior fields are represented by the BIE. Such a relation is provided by the BIE for the external field, and the next system of equations are obtained whose discretization yields:

$$[\Omega]\{\vec{E}_s\}+[\Theta]\{\vec{H}_s\}=\{\vec{b}\} \tag{3.20}$$

where $\{\vec{b}\}$ is a vector related to the incident field and Ω and Θ operators are defined in the next section.

3.3.2 Boundary Integral Formulation (Exterior Region)

Using the Stratton-Chu integral expressions [43], the total fields can then be expressed as:

$$\vec{E}_1(\vec{r}) = \theta_1(\vec{r})\left\{\vec{E}_i(\vec{r}) - \Theta_1\left[\vec{J}_1,\vec{r}\right] + \Omega_1\left[\vec{M}_1,\vec{r}\right]\right\} \quad r \in B_1 \cup \partial B \qquad (3.21)$$

$$\vec{H}_1(\vec{r}) = \theta_1(\vec{r})\left\{\vec{H}_i(\vec{r}) - \Omega_1\left[\vec{J}_1,\vec{r}\right] - \frac{1}{\eta_1^2}\Theta_1\left[\vec{M}_1,\vec{r}\right]\right\} \quad r \in B_1 \cup \partial B \qquad (3.22)$$

$$\vec{E}_2(\vec{r}) = \theta_2(\vec{r})\left\{-\Theta_2\left[\vec{J}_2,\vec{r}\right] + \Omega_2\left[\vec{M}_2,\vec{r}\right]\right\} \quad r \in B_2 \cup \partial B \qquad (3.23)$$

$$\vec{H}_2(\vec{r}) = \theta_2(\vec{r})\left\{-\Omega_2\left[\vec{J}_2,\vec{r}\right] - \frac{1}{\eta_2^2}\Theta_2\left[\vec{M}_2,\vec{r}\right]\right\} \quad r \in B_2 \cup \partial B \qquad (3.24)$$

where η refers to the intrinsic impedance of the mediums, defined as $\eta = \sqrt{\mu/\varepsilon}$, $(\vec{E}_i, \vec{H}_i)$ are the incident fields, and with:

$$\theta_n(\vec{r}) = \begin{cases} 1 & \vec{r} \in B_n \\ 2 & \vec{r} \in \partial B \\ 0 & otherwise \end{cases} \qquad (3.25)$$

where $\theta_n(\vec{r})$ disappears at all points exterior to the surface bounding the volume V, and:

$$\Theta[B,\vec{r}] = \iint_S \left\{ j\omega\mu B(\vec{r}\,') + \frac{j}{\varpi\varepsilon}\left[\nabla' \cdot B(\vec{r})\right]\nabla \right\} G(\vec{r} - \vec{r}\,')ds \qquad (3.26)$$

$$\Omega[B,\vec{r}] = \iint_S B(\vec{r}\,') \times \nabla G(\vec{r} - \vec{r}\,')ds \qquad (3.27)$$

The integrals in the operators Θ and Ω are taken over the boundary ∂B, which encloses the volume V. $G(\vec{r} - \vec{r}\,')$ represents the three dimensional scalar free-space Green's function:

$$G(\vec{r}-\vec{r}\,') = \frac{e^{-j\varpi\sqrt{\varepsilon\mu}\left|\vec{r}-\vec{r}\,'\right|}}{4\pi\left|\vec{r}-\vec{r}\,'\right|} \tag{3.28}$$

where (ε,μ) refers to the permittivity and permeability of the mediums.

In equations (3.21)–(3.24) $\vec{J}_k$ and $\vec{M}_k$ $(k=1,2)$ are related to the tangential field components on the surface ∂B (see Figure 2) by:

$$\hat{n}\times\vec{E}_1 = -\vec{M}_1 \tag{3.29}$$

$$\hat{n}\times\vec{H}_1 = \vec{J}_1 \tag{3.30}$$

$$\hat{n}\times\vec{E}_2 = \vec{M}_2 \tag{3.31}$$

$$\hat{n}\times\vec{H}_2 = -\vec{J}_2 \tag{3.32}$$

with the identification $\vec{E}_1 = \vec{E}^+$, $\vec{E}_2 = \vec{E}^-$, $\vec{H}_1 = \vec{H}^+$, $\vec{H}_2 = \vec{H}^-$, and the continuity condition demands that $\vec{E}^+\times\hat{n} = \vec{E}^-\times\hat{n}$ and $\vec{H}^+\times\hat{n} = \vec{H}^-\times\hat{n}$ where $\hat{n}$ is the unit normal to the surface ∂B.

3.3.2.1 Solutions for Particular Boundary Conditions

The following integral equations in conjunction with the Stratton-Chu integral expressions can be derived depending on the choice of the boundary conditions being applied on surface ∂B, i.e. electric-field integral equation (EFIE), magnetic-field integral equation (MFIE), and the combined field integral equations (CFIE) solutions.

EFIE Solution

The boundary condition for the electric field impinging upon a perfect electric conductor (PEC) is given by:

$$\hat{n}\times\left[\vec{E}_1(\vec{r})-\vec{E}_2(\vec{r})\right]=\hat{n}\times\vec{E}_1(\vec{r})=0 \quad \vec{r}\in\partial B \quad \left(\vec{M}_1\equiv 0\right) \tag{3.33}$$

$$\vec{E}_2=\vec{H}_2\equiv 0\Rightarrow \vec{M}_2=\vec{J}_2\equiv 0 \tag{3.34}$$

using equations (3.21)-(3.27), with the combination of equation (3.33), the EFIE based system of equations are obtained:

$$\hat{n}\times\Theta_1\left[\vec{J},\vec{r}\right]=\hat{n}\times\vec{E}_i(\vec{r}),\ \ \vec{r}\in\partial B \tag{3.35}$$

MFIE Solution

The boundary condition for the magnetic field on a PEC is given by:

$$\hat{n}\times\left[\vec{H}_1(\vec{r})-\vec{H}_2(\vec{r})\right]=\hat{n}\times\vec{H}_1(\vec{r})=\vec{J}(\vec{r}) \quad \vec{r}\in\partial B \quad \left(\vec{M}\equiv 0\right) \tag{3.36}$$

which, in conjunction with equations (3.21)-(3.27), gives the MFIE system of equations:

$$\frac{1}{2}\vec{J}(\vec{r})+\hat{n}\times\Omega_1\left[\vec{J},\vec{r}\right]=\hat{n}\times\vec{H}_i(\vec{r}),\ \ \vec{r}\in\partial B \tag{3.37}$$

CFIE Solution

CFIE solution, which is a linear combination of EFIE and MFIE, is used to alleviate a major drawback experienced when using either the EFIE or the MFIE solution. The linear combination is given by:

$$\alpha EFIE+\eta_1(1-\alpha)\hat{n}\times MFIE \tag{3.38}$$

where α is an arbitrary coefficient that has a of range of $0\le\alpha\le 1$, and the optimum value should be determined. The α parameter is normally set to 0.5.

Dielectric Solution

When dealing with materials that are composed of dielectric materials, dielectric boundaries have to be applied, thus the applicable boundary conditions are:

$$\hat{n}\times\left[\vec{E}_1(\vec{r})-\vec{E}_2(\vec{r})\right]=0 \quad \vec{r}\in\partial B \tag{3.39}$$

$$\hat{n}\times\left[\vec{H}_1(\vec{r})-\vec{H}_2(\vec{r})\right]=0 \quad \vec{r}\in\partial B \tag{3.40}$$

$$\Rightarrow \vec{J}_1=-\vec{J}_2,\ \vec{M}_1=-\vec{M}_2 \tag{3.41}$$

As in the other solutions, using equations (3.21)-(3.27) in conjunction with equations (3.39)-(3.41), the Poggio-Miller-Chu-Harrington-Woo (PMCHW) system of equations are obtained [44]-[47]:

$$\Theta_1\left[\vec{J}_1,\vec{r}\right]+\Theta_2\left[\vec{J}_1,\vec{r}\right]-\Omega_1\left[\vec{M}_1,\vec{r}\right]+\Omega_2\left[\vec{M}_1,\vec{r}\right]=\vec{E}_i(\vec{r}) \tag{3.42}$$

$$\Omega_1\left[\vec{J}_1,\vec{r}\right]+\Omega_2\left[\vec{J}_1,\vec{r}\right]+\frac{1}{\eta_1^2}\Theta_1\left[\vec{M}_1,\vec{r}\right]+\frac{1}{\eta_2^2}\Theta_2\left[\vec{M}_1,\vec{r}\right]=\vec{H}_i(\vec{r}) \tag{3.43}$$

3.3.3 Basis Functions

Once the domain, i.e. inside volume V, is subdivided into smaller volume elements, such as tetrahedral, triangular prisms, hexahedral, rectangular bricks, etc., the proper basis functions has to be introduced, depending on the discretized subdivisions. Since the electric field is the only factor involved in the final finite element formulation, the hexahedral finite element was chosen. In order to solve for $\vec{E}$, the volume V is discretized using a curvilinear hexahedral finite element, which the expansion of $\vec{E}(\vec{r})$ is introduced as:

$$\vec{E}(\vec{r})=\sum_{i=1}^{N}a_i e_i(\vec{r}). \tag{3.44}$$

where a_i are the unknown expansion coefficients, N denotes the number of basis functions used to discretize the domain V, and $e_i(\vec{r})$ are the basis functions defined within the hexahedra.

Any point inside the hexahedron is a parametric mapping of a corresponding point in a unit cube through the transformation:

$$\vec{r}(\vec{u},\vec{v},\vec{w}) = \sum_{i=0}^{2}\sum_{j=0}^{2}\sum_{k=o}^{2} r_{i,j,k} L_{i,j,k}(\vec{u},\vec{v},\vec{w}), \tag{3.45}$$

$$(\vec{u},\vec{v},\vec{w}) \in ([0,1],[0,1],[0,1]). \tag{3.46}$$

where $r_{i,j,k}$ defines the 27 points of the hexahedron (see Figure 3.2) and $L_{i,j,k}(\vec{u},\vec{v},\vec{w})$ are the quadratic Lagrange interpolation functions in the three parameters $(\vec{u},\vec{v},\vec{w})$. The $(\vec{u},\vec{v},\vec{w})$ coefficients are then constructed using the 27 node constraints: $r(0.0,0.0,0.0) = r_{000}$, $r(0.5,0.0,0.0) = r_{100}$, $r(1.0,0.0,0.0) = r_{200}$, … , $r(1.0,1.0,1.0) = r_{222}$.

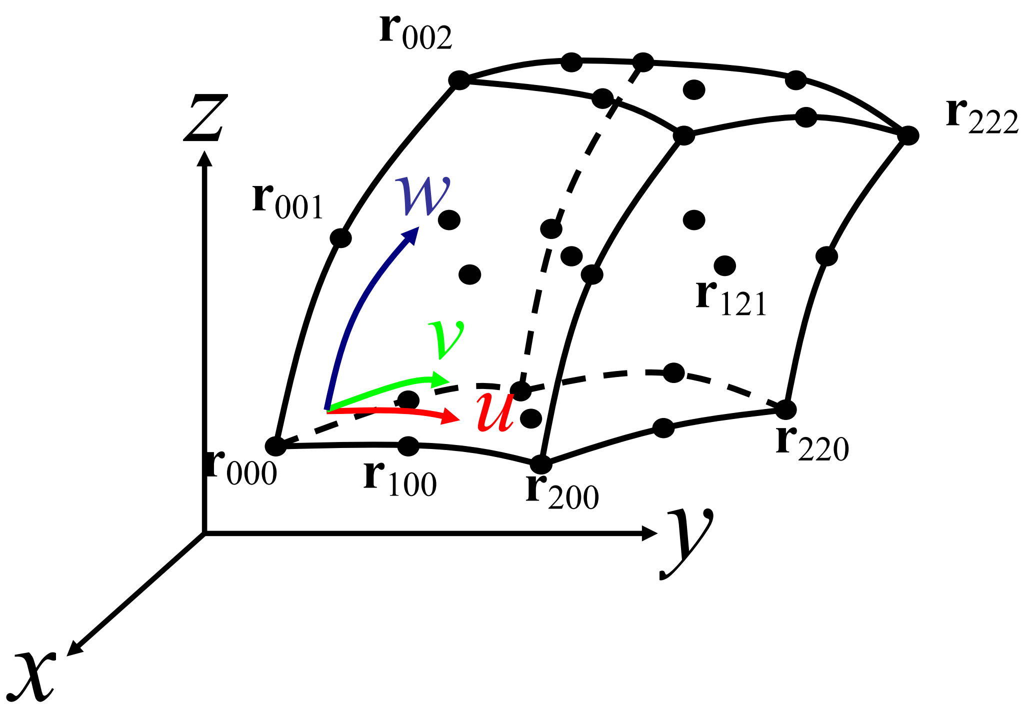

Figure 3.2

A 27 node distorted parametric conformal hexahedron finite element

The defined basis functions in each hexahedron are extensions to those given in [48], which are in terms of the parametric tangent vectors (see figure 3.3). The co-variant projection-edge-based elements are defined as:

$$e^{(u)}(\vec{r}(\vec{u},\vec{v},\vec{w})) = \frac{1}{\sqrt{G}}\frac{\partial \vec{r}}{\partial \vec{u}} \Rightarrow e^{(u)}(\vec{r}(\vec{u},\vec{v},\vec{w})) = \frac{1}{\sqrt{G}}\begin{Bmatrix} 1-\vec{v} \\ \vec{v} \end{Bmatrix}\begin{Bmatrix} 1-\vec{w} \\ \vec{w} \end{Bmatrix}\frac{\partial \vec{r}}{\partial \vec{u}}, \tag{3.47}$$

$$e^{(v)}(\vec{r}(\vec{u},\vec{v},\vec{w})) = \frac{1}{\sqrt{G}}\frac{\partial \vec{r}}{\partial \vec{v}} \Rightarrow e^{(v)}(\vec{r}(\vec{u},\vec{v},\vec{w})) = \frac{1}{\sqrt{G}}\begin{Bmatrix} 1-\vec{u} \\ \vec{u} \end{Bmatrix}\begin{Bmatrix} 1-\vec{w} \\ \vec{w} \end{Bmatrix}\frac{\partial \vec{r}}{\partial \vec{v}}, \tag{3.48}$$

$$e^{(w)}(\vec{r}(\vec{u},\vec{v},\vec{w})) = \frac{1}{\sqrt{G}}\frac{\partial \vec{r}}{\partial \vec{w}} \Rightarrow e^{(w)}(\vec{r}(\vec{u},\vec{v},\vec{w})) = \frac{1}{\sqrt{G}}\begin{Bmatrix} 1-\vec{u} \\ \vec{u} \end{Bmatrix}\begin{Bmatrix} 1-\vec{v} \\ \vec{v} \end{Bmatrix}\frac{\partial \vec{r}}{\partial \vec{w}}. \tag{3.49}$$

where the determinant of the parametric transformation in (3.45)-(3.46) is given by:

$$G = \begin{vmatrix} g_{uu} & g_{uv} & g_{uw} \\ g_{vu} & g_{vv} & g_{vw} \\ g_{wu} & g_{wv} & g_{ww} \end{vmatrix} \tag{3.50}$$

in which:

$$g_{\eta\xi} = \frac{\partial r}{\partial \varsigma} \cdot \frac{\partial r}{\partial \xi}. \tag{3.51}$$

where ς and ξ represent any of the parameters $\vec{u}, \vec{v},$ and $\vec{w}$.

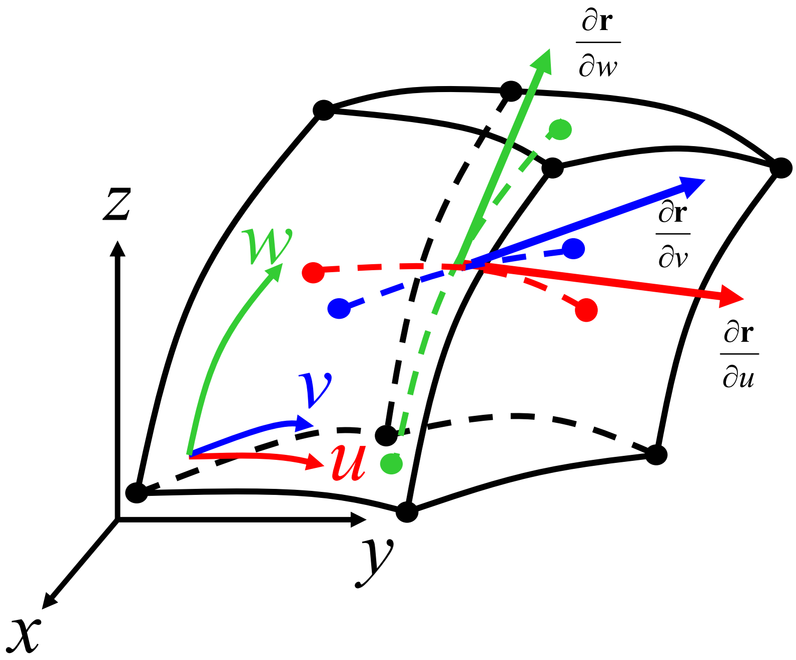

Figure 3.3

Parametric space of hexahedral

The expressions in the terms of the parametric tangent vectors in (3.49) each represent a set of three basis functions for each hexahedron, which has 12 per-element.

An important property of these basis functions is that they have zero divergence inside the hexahedron (in parametric space see Figure 3.3), meaning they are nonzero in the defined hexahedron, but are not directly coupled to the surrounding hexahedra, which is a property that must be satisfied by the electric field intensity $\vec{E}$. The continuity condition of the tangential $\vec{E}$ field is enforced on the boundary by using the BIE above.

CHAPTER IV

KRYLOV SUBSPACE SOLVERS AND PRECONDITIONERS

4.1 Iterative Methods

One of the most powerful tools for solving large and sparse systems of linear algebraic equations is a class of iterative methods called Krylov subspace methods. These iterative methods have a wide range of techniques that use successive approximations to obtain more accurate solutions to a linear system at each step, i.e. solving the $Ax = b$ linear system where A is a $N \times N$ interaction matrix, b is a response vector(s) for the system, and x is the unknown vector(s) to be solved. Efficient and accurate solutions to linear systems are largely a function of the proper choice of an iterative method.

Krylov subspaces are so powerful and successful the method is widely used in the CEM community. Krylov subspaces can be built up using only a function that computes the multiplication of the system matrix and a vector, therefore, the system matrix never has to be formed or stored explicitly. Krylov subspace methods are particularly well suited for applications that are large and have a sparse linear systems. Matrices derived from partial differential equations typically have a number of nonzero elements that are proportional to the matrix size, while the total number of matrix elements is the square of the matrix size. The iterative methods need only to perform a few basic operations per iteration step, which are: vector updates, inner products, matrix vector products, and, if needed, preconditioning.

Krylov subspace methods are mathematically based on projection methods, and the two basic types of projection methods are: the Galerkin (orthogonal residual) method, and the minimal residual (MR) method [49]-[51]. The idea behind these two methods is to approximate the systems’ solution in Krylov subspaces of small dimension instead of solving the potentially very large linear system.

The following is a list of non-stationary Krylov subspace-based iterative solvers that are used in this thesis to solve the linear matrix systems produced by the FE-BI formulation:

Biconjugate Gradient (BICG) Method

This method generates two conjugate-gradient (CG)-like sequences of vectors, one based on a system with the original coefficient matrix and the other on the transpose. Instead of orthogonalizing each sequence, they are made mutually orthogonal, or ``bi-orthogonal". This method, like CG, uses limited storage. It is useful when the matrix is non-symmetric and nonsingular; however, convergence may be irregular, and there is a possibility that the method will break down. BICG requires multiplication with the coefficient matrix and with its transpose at each iteration.

Quasi-Minimal Residual (QMR) Method

This solver was designed to attempt to overcome the irregular convergence behavior of BICG by reducing the tridiagonal system in the least square. QMR takes advantage of the sparse nature of the resulting matrix system. The major advantage of this solver is that it avoids a breakdown by using its look-ahead techniques, and converges smoothly, even though it does not effect a true minimization of either the error or the residual. The computational cost per iteration is slightly higher than BICG, even though it too requires a transpose matrix-vector product.

Conjugate-Gradient Square (CGS) Method

This solver generally converges twice as fast as BICG. The convergence behavior is irregular, which leads to loss of accuracy in the residual update. This method has a similar computational cost as BICG, even though does not require a multiplication with a transpose matrix. The two matrix-vector products are not independent, so the number of synchronization points in a parallel environment is larger.

Biconjugate Gradient Stabilized(l) (BICGSTAB(l)) Method

This solver is a modification of BICG, which solves nonsymmetric linear systems while avoiding the irregular convergence patterns of the CGS, and raises the efficiency of BICG. An advantage of this method is that it requires no transpose matrix, but instead requires two matrix-vector products and four inner products. BICGSTAB(l) often converges twice as fast as the BICG. Since the residual vector is minimized, at least locally, it results in a significantly smoother convergence behavior. The (l) parameter in BICGSTAB(l) is the degree of the minimal residual polynomials. The higher the (l) parameter number, the lower the iteration number, faster the convergence, but with higher computational cost. This solver is ideal to use in FE-BI analysis, since the solver breaks down in the case where the coefficient matrix has eigenvalues close to the imaginary axis. This is prominent, since the FE-BI method results in a complex-valued non-symmetric matrix, which is likely to have eigenvalues close to the imaginary axis.

4.2 Krylov Subspaces

In this section, a brief mathematical description background of the Krylov subspace methods is introduced for solving linear algebraic systems of the form:

$$Ax = b, \tag{4.1}$$

where A is a real or complex nonsingular $N \times N$ matrix, b is a real or complex vector of length, N. Suppose that x_0 is an initial guess for the solution of x, and the initial residual is defined as $r_0 = b - Ax_0$. The Krylov subspace methods can be derived from the following projection method, as originally shown by Saad [52]-[54], the nth iterate x_n, $n = 1,2,\ldots,$ is of the form:

$$x_n \in x_0 + S_n, \tag{4.2}$$

where S_n is some n-dimensional space called the "search space". The solution of x_n can be made unique by the constraint of n, since n has a degree of freedom. This is accomplished by choosing an n-dimensional space C_n, called the "constraint space", and by requiring that the nth residual is orthogonal to that space [55], i.e.,

$$r_n = b - Ax_n \in r_0 + AS_n, \qquad r_n \perp C_n \tag{4.3}$$

The two basic relations between S_n and C_n in two of the most popular used Krylov subspace method are:

$$C_n = S_n \qquad \text{(Galerkin method)} \tag{4.4}$$

$$C_n = AS_n \qquad \text{(Minimal residual method (MR))} \tag{4.5}$$

The Galerkin and the MR methods are so called a "Krylov subspace method," when Krylov subspace $K_n(A, r_0)$ are used as search spaces. In other words:

$$S_n = K_n(A, r_0) \equiv span\{r_0, Ar_0, \ldots, A^{n-1}r_0\}, \qquad n = 1,2,3,\ldots.. \tag{4.6}$$

In the background of Krylov subspaces, the Galerkin method is usually described as an orthogonal residual (OR) method since using, (4.6) as spaces in the Galerkin method, the residuals are constructed as $r_n = b - Ax_n$, which are orthogonal to all previous residuals $r_{n-1}, \cdots, r_0$.

The Krylov subspaces form a nested sequence that ends with a subspace of maximal dimension $d = \dim K_N(A, r_0)$, i.e.,

$$K_1(A, r_0) \subset \cdots \subset K_d(A, r_0) = \cdots = K_N(A, r_0) \tag{4.7}$$

The number of steps of the OR/MR Krylov subspace method is bounded by the maximal Krylov subspace dimension *d*. It is noted that a projection process breaks down in step *n* if no iterate x_n exists, or if x_n is not unique [56]. This break down process is determined and dependent on how well defined the method is and the properties of the *A* matrix [55].

In general, the OR Krylov subspace method yields uniquely defined iterates for each *n*, whenever zero is outside the *field of values* of *A*, which is defined as:

$$F(A) = \{v^H Av : v^H v = 1, \ v \in C^N\} \tag{4.8}$$

The conditions $x_n \in x_0 + K_n(A, r_0)$ and $r_n \in r_0 + AK_n(A, r_0)$ imply that the error $x - x_n$ and the residual r_n can be written in the polynomial form of:

$$x - x_n = p_n(A)(x - x_0), \tag{4.9}$$

$$r_n = p_n(A)r_0, \tag{4.10}$$

where p_n is a polynomial of degree *n*, and with a value of one at the origin. The polynomial p_n is distinctively determined by the constraint condition of (4.3) for a well-defined OR/MR Krylov subspace method [55].

4.3 Preconditioners

There are many instances and applications where iterative methods fail to converge or converge slowly. The rate at which an iterative method converges depends greatly on the spectrum of the coefficient matrix. Hence, iterative methods usually involve a second matrix that transforms the coefficient matrix into one with a more favorable spectrum. The transformation matrix is called a *preconditioner*, that is, instead of solving $Ax = b$, one solves $MAx = Mb$, or a spectrally equivalent system (where *M* is the linear operator preconditioner). A good preconditioner improves the convergence of the iterative method sufficiently to overcome the extra cost of constructing and applying the preconditioner. Indeed, without a preconditioner, the iterative method may fail to converge. To identify a proper and efficient preconditioner, the next three properties are normally taken into account:

- *M* is a good approximation to *A*.
- The cost of the construction of *M* is not prohibitive.
- The system $My = z$ is much easier to solve than the original matrix system.

The efficiency of a preconditioner normally signifies that the iterative method selected to solve the matrix system problem converges much faster in terms of CPU time, without consuming a large trade-off amount of CPU memory. The primary role of an applied preconditioner for Krylov subspace iterative methods is the reduced condition number and/or enhanced eigenvalue distributions for the preconditioned matrices.

The following preconditioner is the most popular and generally used to help iterative solvers gain convergence speed and/or transform a non-convergent system into a convergent one:

Incomplete Factorization (ILU)

A broad class of preconditioners is based on incomplete factorizations of the coefficient matrix. This preconditioner is called “factorization incomplete” if, during the factorization process, certain *fill* elements, and/or nonzero elements in the factorization in positions where the original matrix had a zero, have been ignored. This type of preconditioning is one of the most commonly applied methods. In this method, some sparse approximation of the exact L and U factors, namely L and U, in the LU factorization of A, is first obtained, and then used as preconditioning matrices in the iterative process. This preconditioner is then given in factored form $M = LU$, with L as a lower and U as an upper triangular. The efficacy of the preconditioner depends on how well M^{-1} approximates A^{-1}. These methods, although very much effective in increasing the rate of convergence, suffer from an important drawback, which is related to possibility of breakdowns during an incomplete factorization process, due to the occurrence of (almost) zero pivots or indefinite matrices (negative pivots) even if the full factorization of the same matrix is guaranteed to exist and yield a positive definite matrix.

CHAPTER V

WIRELESS MEDICAL TELEMETRY APPLICATIONS

5.1 Medical Telemetry Application

There are many electrical characteristics that must be considered when designing an implantable antenna for wireless medical telemetry applications. The two basic antenna characteristics necessary for this application is the radiation patterns and the input impedance (return loss). The radiation pattern consists of co- and cross-polarization, axial ratio, and gain. The input impedance consists of the resonant resistance and the bandwidth at the operating frequency. These design considerations have led antenna designers to consider a limited number of antenna structures that will be suitable for in-vivo applications. Other important parameters that must be accounted for when designing an implantable antenna are the medium properties, in this case the human body. This is very difficult to simulate because the human body is a lossy medium. The two main factors that affect the body tissue are the relative permittivity and conductivity. These parameters change constantly from person to person depending on the individual physiological structure, (i.e. slim, overweight, hydrated, dehydrated, etc.) and are frequency dependent.

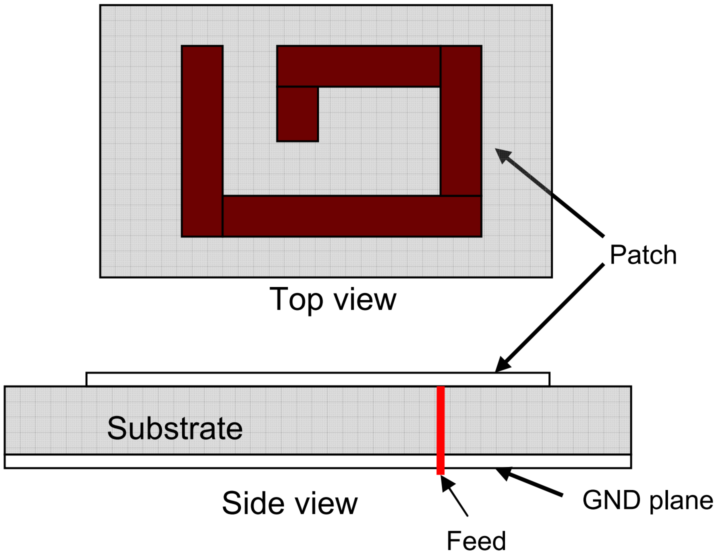

Figure 5.1

Conventional microstrip antenna

The conventional printed microstrip antennas (see Figure 5.1) do not fulfill many of the requirements of a miniature antenna for implantable applications. A small size antenna, meaning "electrically small", is where the extent of the antenna structure is much, much less than a wavelength λ. However, these antennas have many design parameters that could be optimized to reduce their size, cost, increase their bandwidth, make them sensitive to different polarizations, improve their radiation characteristics, and enhance the Q factor. One technique used to reduce the size of the conventional microstrip antenna is by placing a shorting pin from the radiator to the ground plane. This procedure provides the same resonant frequency at less than half the size of a conventional microstrip antenna. Another technique used to increase the bandwidth and enhance the gain efficiency of the antenna is to add a superstrate with a certain thickness and relative permittivity of high value. One popular example is the planar inverted-F antenna (PIFA) for these types of procedures. The antenna is called an inverted-F antenna because when seen from the side view, the antenna (see Figure 5.2) resembles an upside down letter F.

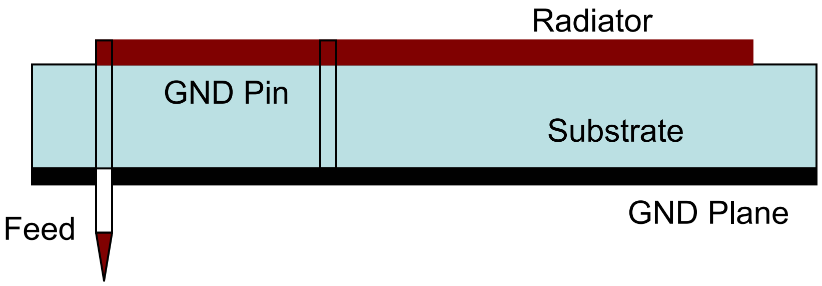

Figure 5.2

Side view of a planar inverted-F antenna (PIFA)

The superstrate cover is often used to protect the radiating element (radiator) against the environment, as in implantable antennas. The loading of the superstrate cover reduces the resonant frequency, decreases the resonant resistance, and enhances the impedance bandwidth of a microstrip antenna. The larger the relative permittivity of the superstrate is, the more the resonant frequency goes down as the superstrate becomes thicker. Similar to the behavior of the resonant frequency as the superstrate thickness and relative permittivity changes, the resonant resistance is decreased. The larger the relative permittivity of the superstrate is, the more the resonant resistance is decreased. An optimal superstrate thickness can be found to get the maximum bandwidth with respect to the superstrate relative permittivity. The larger the superstrate relative permittivity is, the larger the maximum bandwidth that can be obtained.

In subsections 5.3 and 5.4, two printed microstrip antennas, a spiral and a serpentine, will be closely evaluated for the application of medical telemetry as an implantable antenna. Both of the antennas mentioned above can be characterized as PIFAs', since they take the conventional side view look of an F when the short pin is added. The PIFA can generally be regarded as an omni-directional, low profile antenna with narrow bandwidth, low input resistance, high reactance, and low radiation efficiency. Thus, an optimum design must be met with all the proper properties dealing with the antenna and the medium it will be embedded in.

The first set of simulated results is an antenna design in an air environment. This is done to verify the FE-BI computational results using a non-stationary Krylov subspace solvers. This step will also determine which solver is best suited for this sort of application. Then, the spiral and serpentine antennas are redesigned and simulated, this time while encased in a protective housing and embedded in a block of skin and/or fat tissue, using the same FE-BI procedure. The parameters of the antennas: near field distribution, far field radiation pattern, return loss, voltage standing wave ratio (VSWR), are presented along with the convergence behavior of the applied solver.

5.2 Design Specifications

When dealing with an in-vivo design application, the relevant parameters of the medium, in this case human tissue, and the antenna specifications must be consider. The tissue parameters from 402 MHz to 405 MHz are researched first, which the values were retrieved from the data compiled by C. Gabriel and William D. Hurt at Armstrong Laboratory, Brooks AFB [56]-[58]. Table 5.1 shows the parameter values for the relevant tissues at frequency of 402 MHz. The antenna specifications for the implantable design are given in Table 5.2.

Table 5.1

Electrical properties of human tissue

Electrical Properties of Human Body Tissues (402-405 MHz)					
Tissue	**Properties**	**402 MHz**	**403 MHz**	**404 MHz**	**405 MHz**
Bone	ε_r **(Relative Permittivity)** σ **(Conductivity, S/m)** ρ **(Mass Density, 10^3 kg/m^3)**	**13.143** **0.091514** **1.81**	**13.14** **0.091603** **1.81**	**13.138** **0.091691** **1.81**	**13.136** **0.09178** **1.81**
Muscle	ε_r **(Relative Permittivity)** σ **(Conductivity, S/m)** ρ **(Mass Density, 10^3 kg/m^3)**	**57.112** **0.79682** **1.04**	**57.104** **0.79708** **1.04**	**57.096** **0.79734** **1.04**	**57.088** **0.79759** **1.04**
Blood	ε_r **(Relative Permittivity)** σ **(Conductivity, S/m)** ρ **(Mass Density, 10^3 kg/m^3)**	**64.16** **1.3503** **1.06**	**64.149** **1.3506** **1.06**	**64.138** **1.3509** **1.06**	**64.127** **1.3513** **1.06**
Fat	ε_r **(Relative Permittivity)** σ **(Conductivity, S/m)** ρ **(Mass Density, 10^3 kg/m^3)**	**5.5789** **0.041151** **0.92**	**5.5785** **0.041167** **0.92**	**5.5781** **0.041183** **0.92**	**5.5777** **0.041199** **0.92**
Skin	ε_r **(Relative Permittivity)** σ **(Conductivity, S/m)** ρ **(Mass Density, 10^3 kg/m^3)**	**46.741** **0.68892** **1.01**	**46.718** **0.68934** **1.01**	**46.695** **0.68977** **1.01**	**46.672** **0.6902** **1.01**

Table 5.2

Antenna specifications

Frequency Range	**402-405 MHz (MICS Band)**
Impedance	**50 Ohms**
Return Loss	**Less than -10 dB**
VSWR	**Less than 2:1 Nominal**
Radiation Pattern	**Omni-directional**
Polarization	**Circular**

5.3 Code Validation

To validate our FE-BI code, the comparisons with MoM results was given for a rectangular PEC box (see Figure 5.3). The PEC box was excited by a plane wave along the z-axis. As seen Figure 5.4, there is a good agreement between the two techniques. The MoM data was taken from [59].

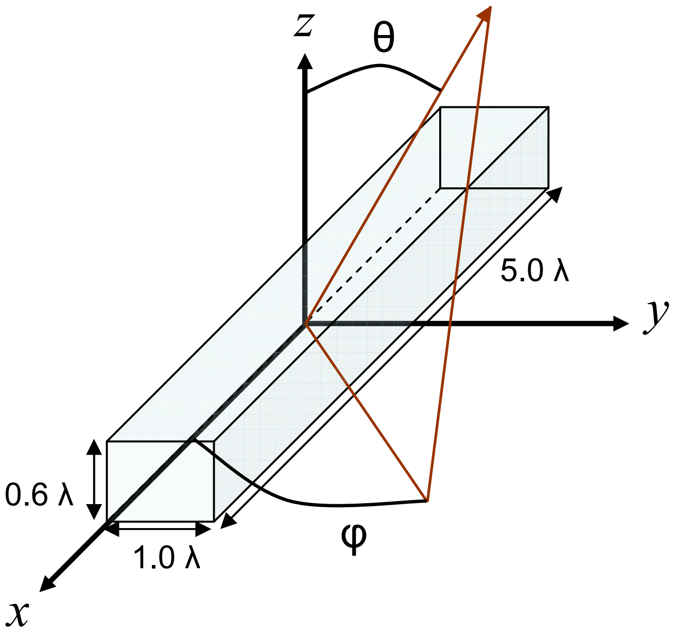

Figure 5.3

PEC box dimension $5.0\lambda \times 1.0\lambda \times 0.6\lambda$

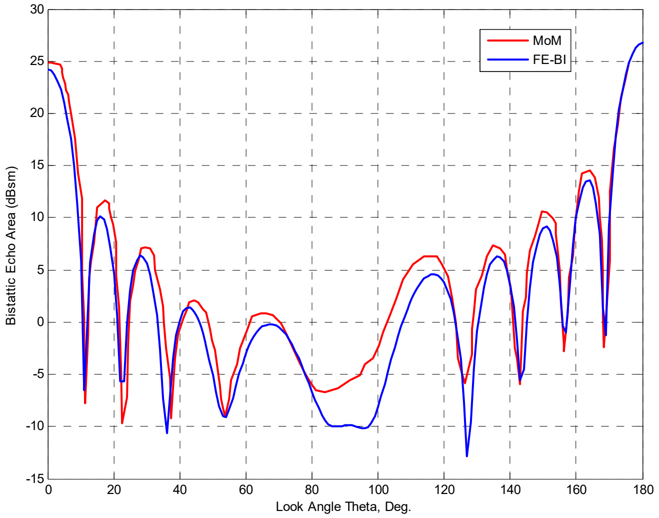

Figure 5.4

Echo area for $5.0\lambda \times 1.0\lambda \times 0.6\lambda$ of PEC box

5.4 Spiral Antenna

The spiral antenna, presented here, is not a true conventional spiral antenna. The antenna is more like a planar monopole antenna wrapped around the substrate once. Figures 5.3 and 5.4 shows one of the geometries of the PIFA spiral antennas studied in this thesis. The next two sections present two different types of spiral antennas. One of the antennas is designed to operate in an outside environment (air) for the MICS band still emphasizing a relatively small structure, and the other one is designed for the embedded system, which will be encased and placed in a block of skin.

5.4.1 Single Spiral Antenna

Figures 5.5 and 5.6 show the top and side view, respectively, of the geometry of the microstrip spiral antenna design for the air environment. The dimensions, all units in millimeters, of the antenna are shown. In order to evaluate the solvers for the three-dimensional FE-BI method, this antenna was designed for the MICS band in air. The microstrip spiral antenna covers the substrate with a superstrate. The substrate material is composed of gallium-arsenide while the superstrate is a Rogers RO4232 (TM) material. The substrate has a relative permittivity of 12.9 and the superstrate has a relative permittivity of 3.2 with the loss tangent of 0.0018.

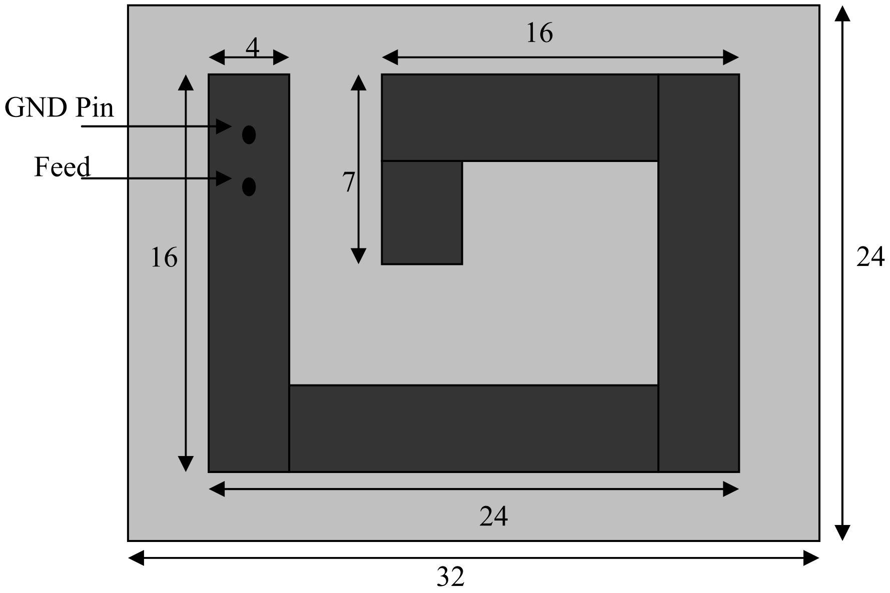

Figure 5.5

Top view of spiral antenna

Figure .5.6

Side view of spiral antenna

Figure 5.7 shows the discretized (mesh) geometry of the spiral antenna. The mesh has a total of 510 hexahedral elements with 5,425 nodes, and an edge length of less than λ/25 for the frequency of 403 MHz. It has a total of 2,936 unknowns, which 1,660 unknowns come from the FEM analysis and 1,276 unknowns comes from the BI analysis.

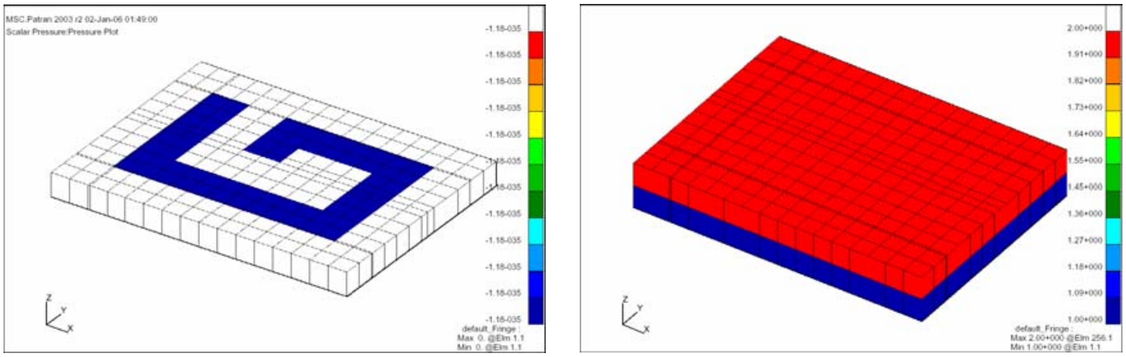

(a) (b)

Figure 5.7

Discretized spiral antenna (a) substrate and (b) superstrate

The evaluation of the GMRES, BICG, CGS, and BICGSTAB solvers are carried out and summarized in Table 5.3, with the tolerance set to 0.01. The computation of the tolerance is the Euclidean norm, which the norm gives a measure for the distance from the vector(x) to the original vector(0). A noticeable difference can be seen in the decrease of iteration number when different solvers are employed. The dominant solver was the BICGSTAB, which reduced the amount of the iteration over 70%. The memory consumption was monitored as well while the simulations were being carried out. There was not a significant difference in the memory usage when using the different solver for this application.

Table 5.3

Total number of iterations and memory usage for different solvers.

Tolerance = 0.01		
Solver	**Iteration Number**	**Memory Usage (MB)**
GMRES	**5961**	**35.092**
BICG	**3180**	**35.196**
CGS	**7727**	**35.140**
BICGSTAB	**1654**	**35.184**

Since the BICGSTAB was the dominant solver, the evaluation of the l parameter in the BICGSTAB(l) will be studied. When the l parameter is set to 1, the solver reduces back to the regular BICGSTAB solver. Table 5.4 shows the total number of iterations and total amount of memory consumed for the BICGSTAB(l = 2,4,8,12) solver. Figure 5.8 shows the graphs of the iteration number with respect to the residual error, graphically showing the performance of the solver. As seen from the computed results, when the l parameter increased, the total number of iterations decreased for all cases. The disadvantage of the solver is when the l parameter is increased, the memory requirement also increases even though the iteration number is lower substantially. The results clearly show that the BICGSTAB(l) solver is superior to all other solvers for all the runs in this application. Thus the use of this solver will be carried out through out the rest of the thesis.

Table 5.4

Total number of iterations and memory usage for BICGSTAB(l) solvers.

Tolerance = 0.01		
Solver	**Iteration Number**	**Memory Usage (MB)**
BICGSTAB(2)	**1642**	**35.292**
BICGSTAB(4)	**1254**	**35.480**
BICGSTAB(8)	**311**	**35.848**
BICGSTAB(12)	**19**	**36.216**

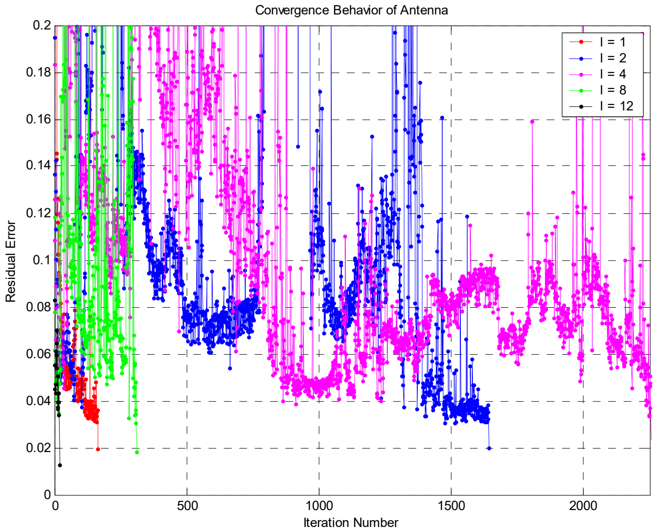

Figure 5.8

Convergence behavior of BICGSTAB(l) solver with spiral antenna

Figure 5.9 show the return loss of the spiral antenna. The FE-BI and HFSS results are placed on top of each other to illustrate the validation of the FE-BI code. As seen in the return loss graph, the input impedance for both results is below -10 dB. The FE-BI algorithm computed the return loss at -13.93 dB with a bandwidth of 0.834 % and a minimum (with respect to return loss) at 402.6 MHz, and HFSS calculated the return loss at -21.08 dB with a bandwidth of 1.072 % and a minimum at 404.1. The discrepancies between both results are likely over numerical error.

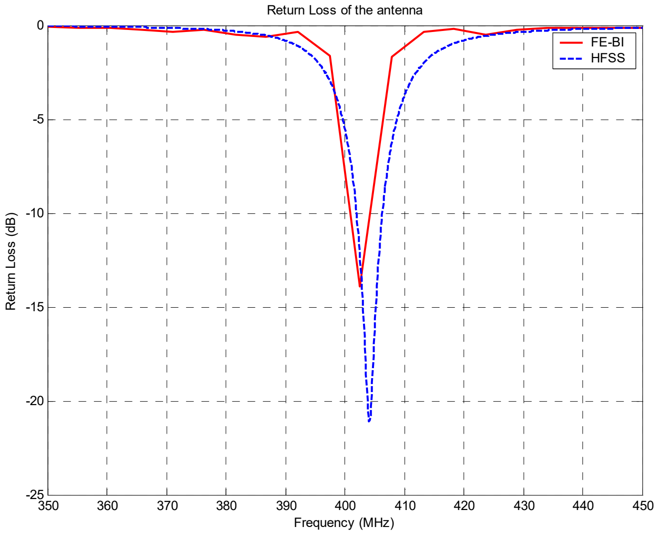

Figure 5.9

Return loss of spiral antenna

Figure 5.10 displays the electric and magnetic co- and cros-pol far field radiation. From this graph the omni-directional radiation pattern can be clearly seen. Figure 5.11 displays the near field distribution of the electric field with and without the superstrate. The red coloration signifying the hot spots of the antenna.

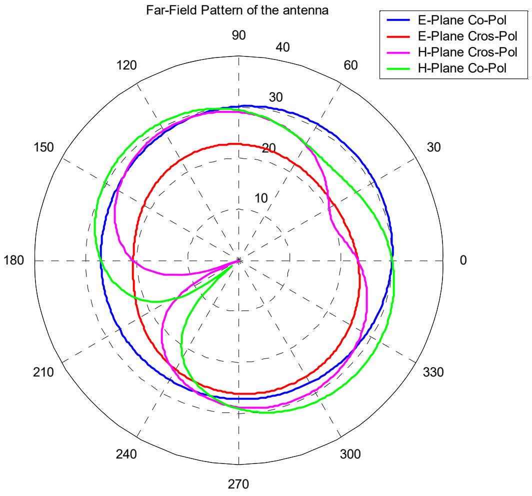

Figure 5.10

Far-field radiation patterns E(x,y) and H(x,y) of spiral antenna

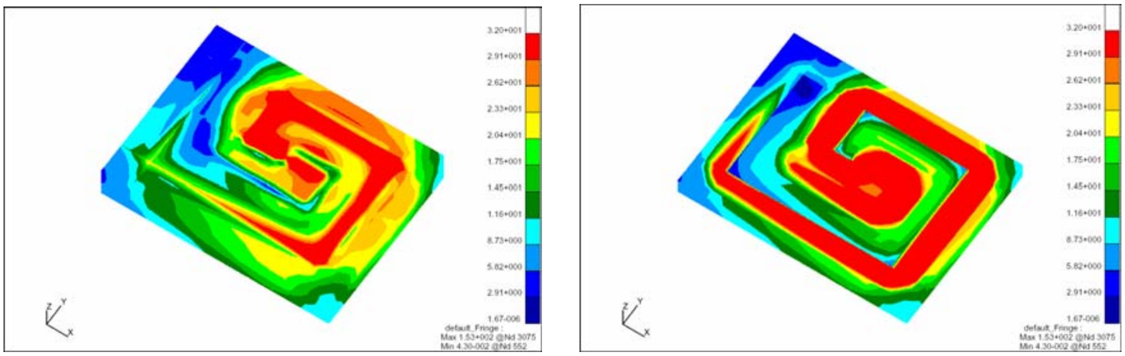

(a) (b)

Figure 5.11

Near field distribution of spiral antenna with (a) superstrate and (b) without superstrate at 402 MHz

5.4.2 Spiral Antenna Embedded in Skin

In this section, the microstrip spiral antenna, operating from the frequency 402 MHz to 405 MHz, is designed for the embedded system. The antenna, as seen in Figure

5.12 and 5.13 with all the dimension in millimeters, consists of a wrapped planar monopole shaped radiator between the substrate and superstrate. The substrate and superstrate are composed of the same material, silicon, which has a relative permittivity of 11.9. The antenna is encased in silicon in order to reduce and prevent the surrounding tissue from heating and to prevent shorting of the system. The silicon material was chosen for the encasement since it is a biocompatible material. The antenna is then placed in the middle of a box imitating a finite piece of skin. The proper properties, permittivity and conductivity, of the skin (Table 5.1) are accounted for.

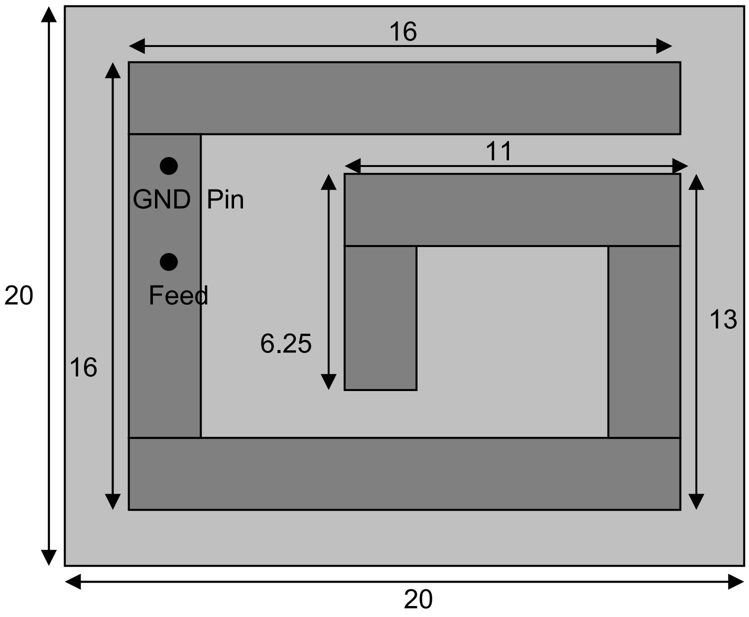

Figure 5.12

Top view of embedded spiral antenna

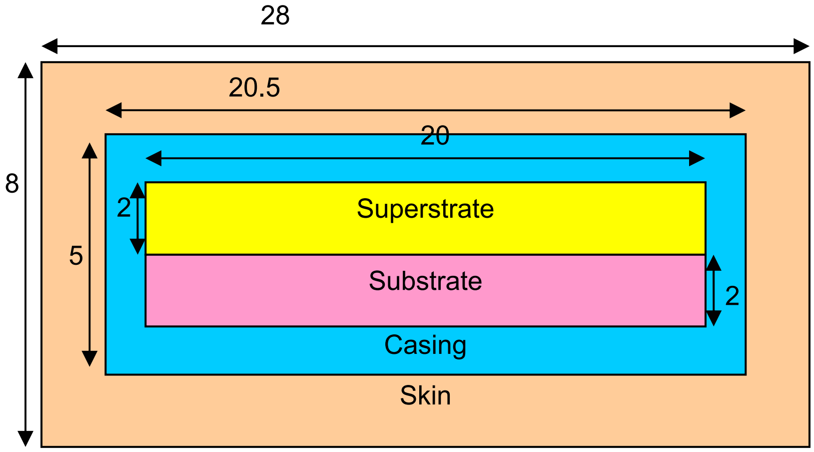

Figure 5.13

Side view of embedded spiral antenna

Figure 5.14 show the return loss of the embedded spiral antenna. A validation is carried out for the design in HFSS as well. The return loss from the FE-BI result is shifted to the right by 4 MHz with a resonating frequency of 410.1 MHz at -10 dB, which basically has a 0% bandwidth. An advantage this application has is that it will be used for short range. The approximate range used will be 0.5 to 2 meters, so the return loss is still acceptable as long it does not rise above -7 dB. HFSS calculated the return loss at -18.05 dB with a bandwidth of 2.494 % and a minimum at 401.7. The discrepancies, as in the last section, are due to numerical error. In this design though, the evaluation of the different boundary conditions composed of different dielectric and inhomogeneous regions raise the numerical error when solving for the fields in the different areas.

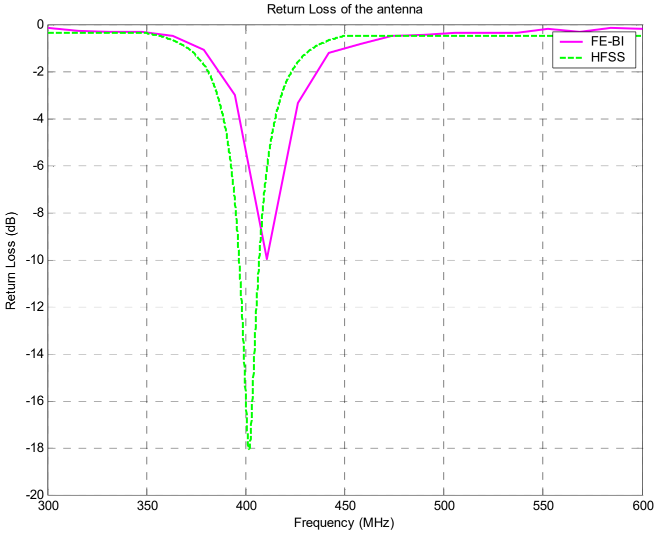

Figure 5.14

Return Loss of embedded spiral antenna

Figure 5.15 displays the electric and magnetic co- and cros-pol far field radiation. The omni-directional radiation pattern is still achieved with a slight degrading change to the co-polarization pattern, which was expected from the effect of the high permittivity and the conductivity of the surrounding environment. Figure 5.16 displays the VSWR for the antenna. As seen from the graph, the VSWR reaches the 2:1 nominal ratio.

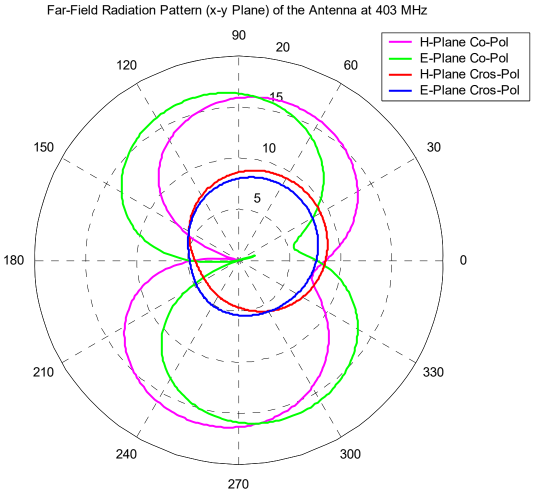

Figure 5.15

Far-field radiation pattern (x-y plane) of embedded spiral antenna

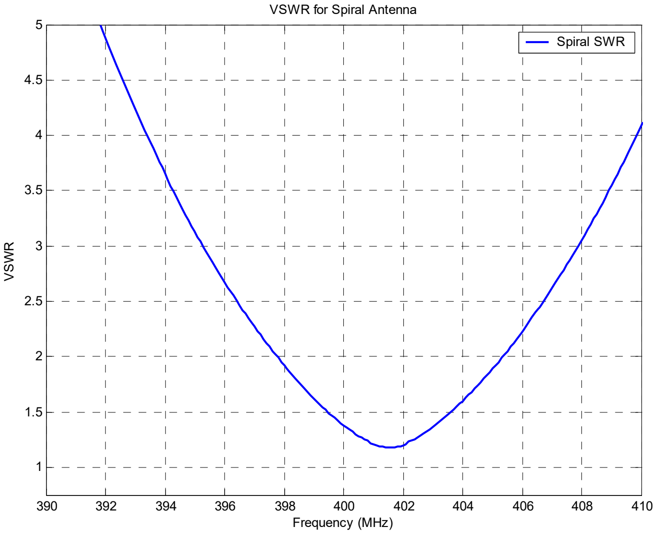

Figure 5.16

VSWR for embedded spiral antenna

The convergence behavior is seen in Figure 5.17 with the BICGSTAB(8) solver. As seen, the iteration number is low and converged smoothly with a set tolerance of 0.02. Figure 5.18 displays the near field distribution of the electric fields at four different locations. The first location illustrates the fields on top of the skin, the second on the silicon encasement, the third on the silicon superstrate, and the last on top of the silicon substrate. The near field distribution shows the intensity of electric fields in the surrounding environment with the red coloration signifying the hot spots. Figure 5.18 (a) shows the hot spots on the skin with the maximum field intensity of 0.3 V/m while Figure 5.18 (b)-(d) shows the hot spots on the encasement, superstrate, and substrate, respectively with the maximum field intensity at 25 V/m. The scale was raised for the last three figures to demonstrate the near field pattern and design configuration.

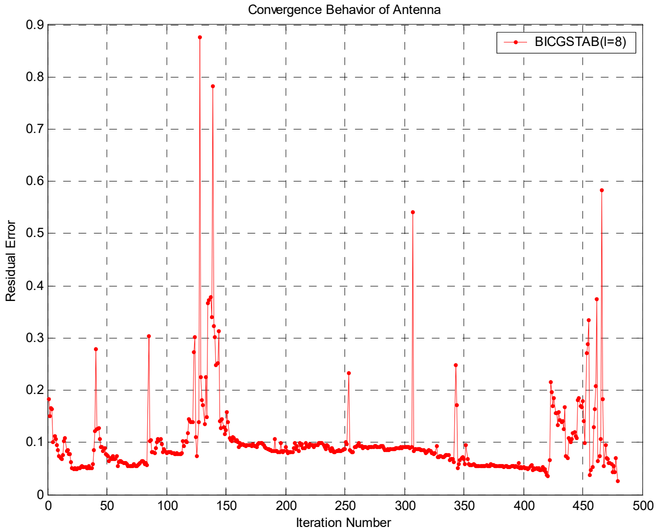

Figure 5.17

Convergence behavior of embedded spiral antenna for BICGSTAB(8)

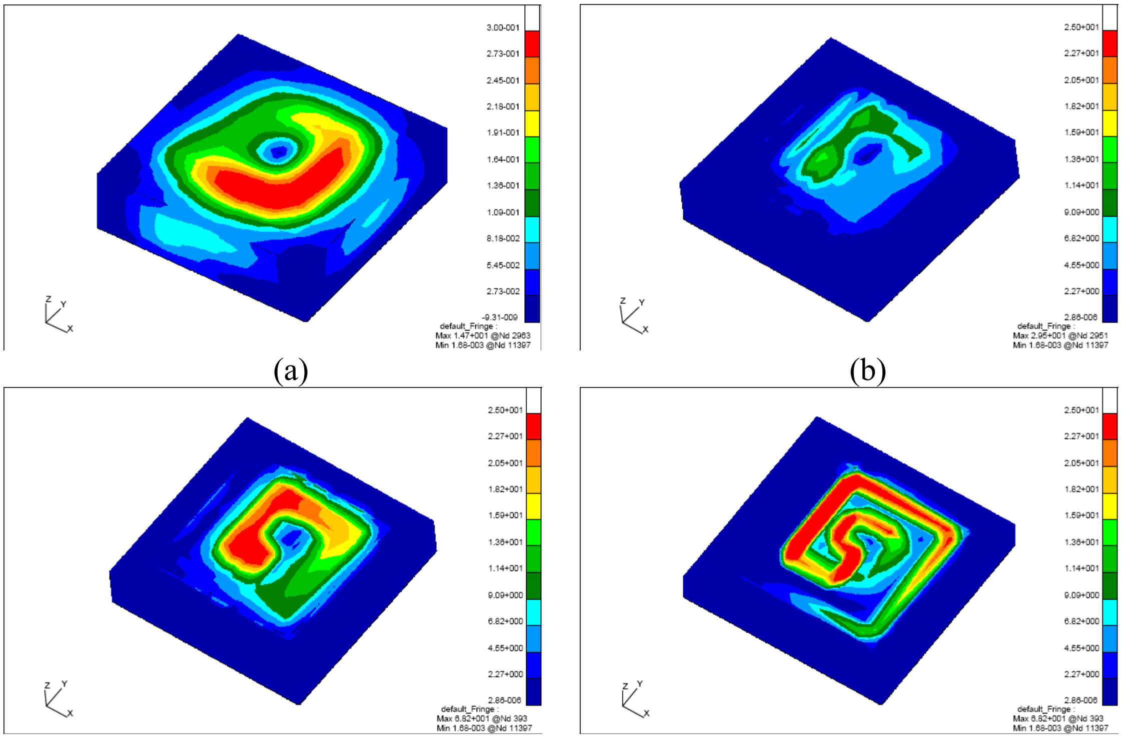

(a) (b)

(c) (d)

Figure 5.18

Near field distribution of embedded spiral antenna, (a) top of skin (b) casing, (c) superstrate, and (d) substrate

5.5 Serpentine Antenna Embedded in Skin

In this section, the serpentine antenna operating in the MICS band is presented. The antenna, as shown in Figure 5.19 and 5.20 with all the dimension in millimeters, consists of a serpentine shaped radiator in between the substrate and superstrate. The substrate and superstrate are composed of the same material, gallium-arsenide, which has a relative permittivity of 12.9. The antenna is encased in silicon in order to reduce the compromise of the tissue and prevent form shorting out the system. As before, the silicon material was chosen for the encasement since it is a biocompatible material.

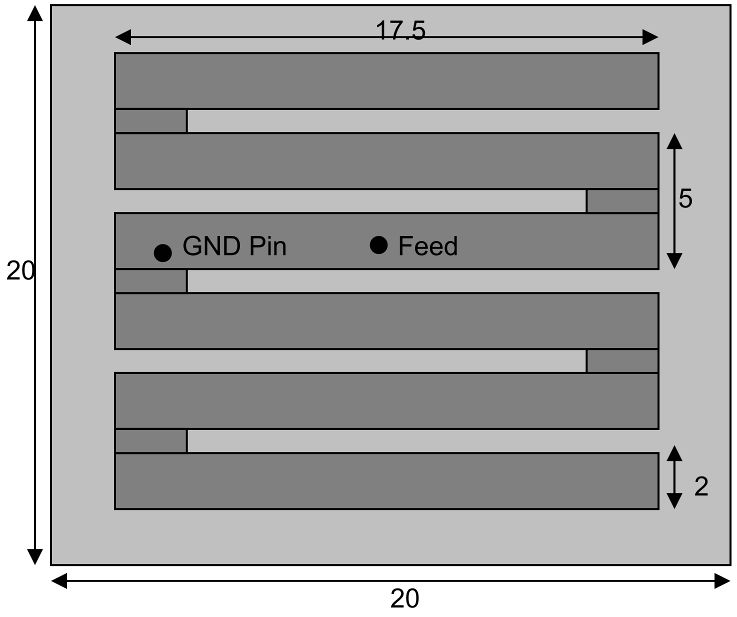

Figure 5.19

Top view of embedded serpentine antenna

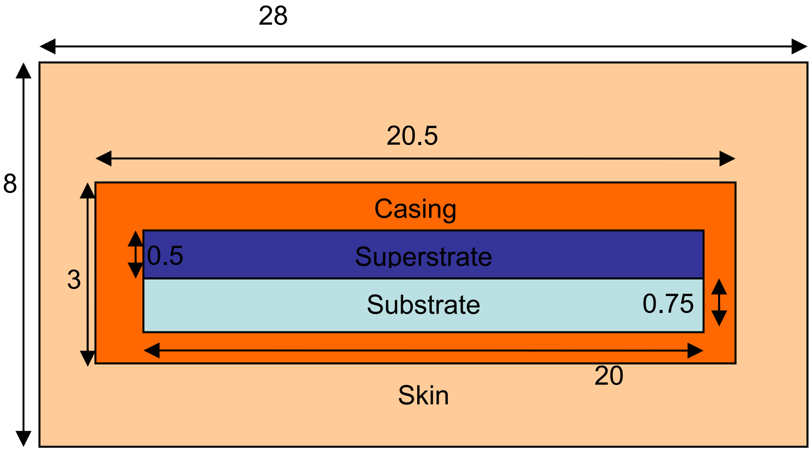

Figure 5.20

Side view of embedded serpentine antenna

Figure 5.21 shows the return loss of the embedded serpentine antenna. A comparison is done with HFSS to verify the results. The return loss from the FE-BI result is slightly shifted to the right by 5 MHz with a resonating frequency of 406.1 MHz at -10 dB, which basically has a 0% bandwidth. As explained in the embedded spiral antenna section, the advantage in this application is that the return loss is acceptable as long as it does not rise above -7 dB. HFSS computed the return loss at -19.53 dB with a bandwidth of 1.899 % and a minimum at 402.3. The similar discrepancies are seen for this antenna as the spiral, a slight shift to the right with a reduction of 5 to 7 dB in the return loss.

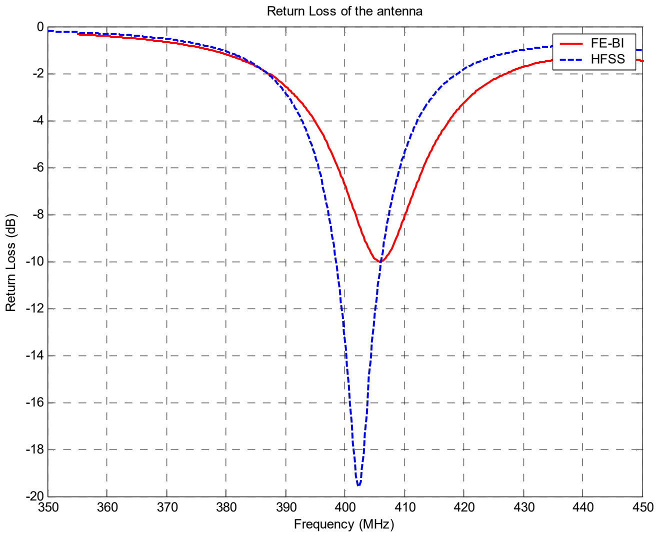

Figure 5.21

Return loss of embedded serpentine antenna

Figure 5.22 displays the electric and magnetic co- and cros-pol far field radiation. The omni-directional radiation pattern is still achieved with a slight degrading change to the co-polarization pattern as in the spiral antenna. Figure 5.23 displays the VSWR for the antenna. As seen from the graph, the VSWR reaches the 2:1 nominal ratio.

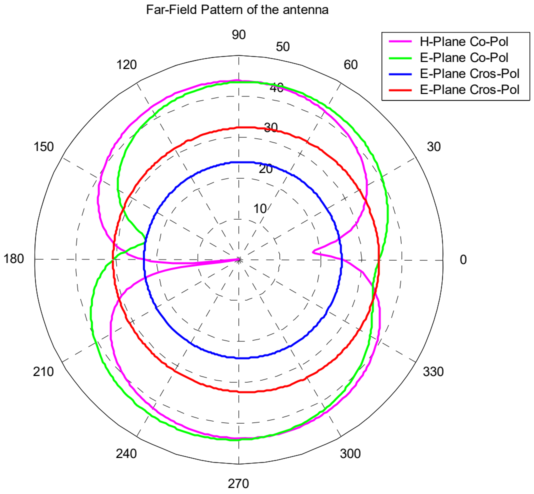

Figure 5.22

Far-field radiation pattern (x-y plane) of embedded serpentine antenna

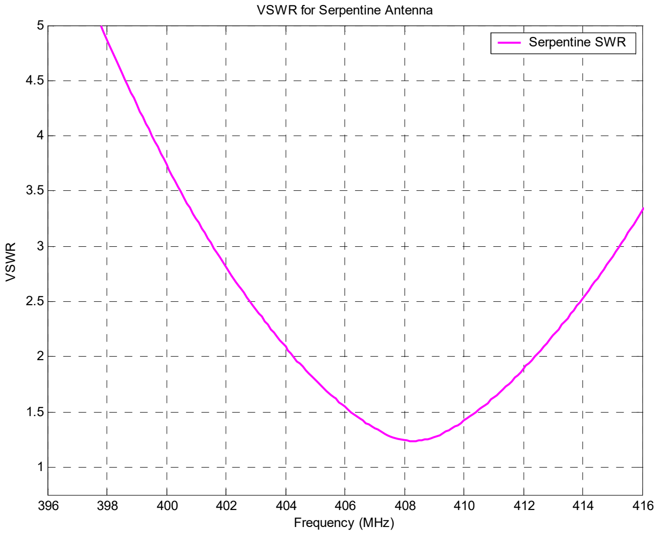

Figure 5.23

VSWR for embedded serpentine antenna

The convergence behavior for the embedded serpentine antenna is displayed in Figure 5.24 with the BICGSTAB(8) solver. The iteration number is moderately high, which has about 3 times more iterations than the embedded spiral antenna with the same set tolerance of 0.02. Figure 5.25 displays the near field distribution of the electric fields at the same four locations as the embedded spiral antenna. The first location illustrates the fields on top of the skin, the second on the silicon encasement, the third on the gallium-arsenide superstrate, and the last on top of the gallium-arsenide substrate. Figure 5.25 (a) shows the hot spots on the skin with the maximum field intensity of 0.3 V/m while Figure 5.25 (b)-(d) shows the hot spots on the encasement, superstrate, and substrate, respectively with the maximum field intensity at 25 V/m. There are less visible hot spots on the skin from the serpentine antenna than from the spiral antenna while the encasement, superstrate, and substrate exhibits more hot spots than the spiral antenna.

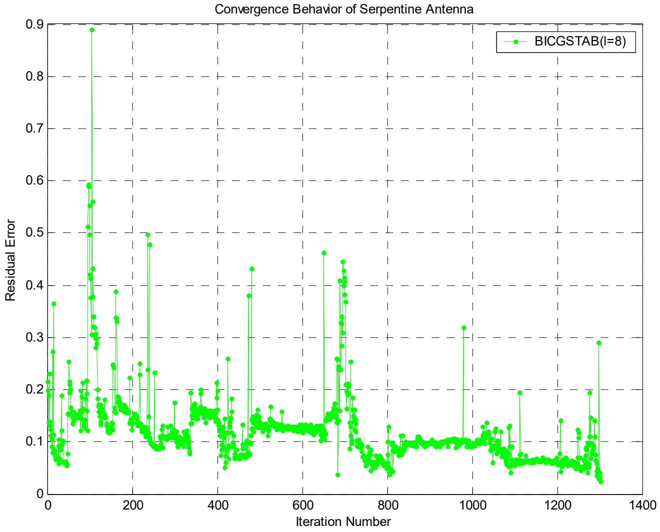

Figure 5.24

Convergence behavior of embedded serpentine antenna for BICGSTAB(8)

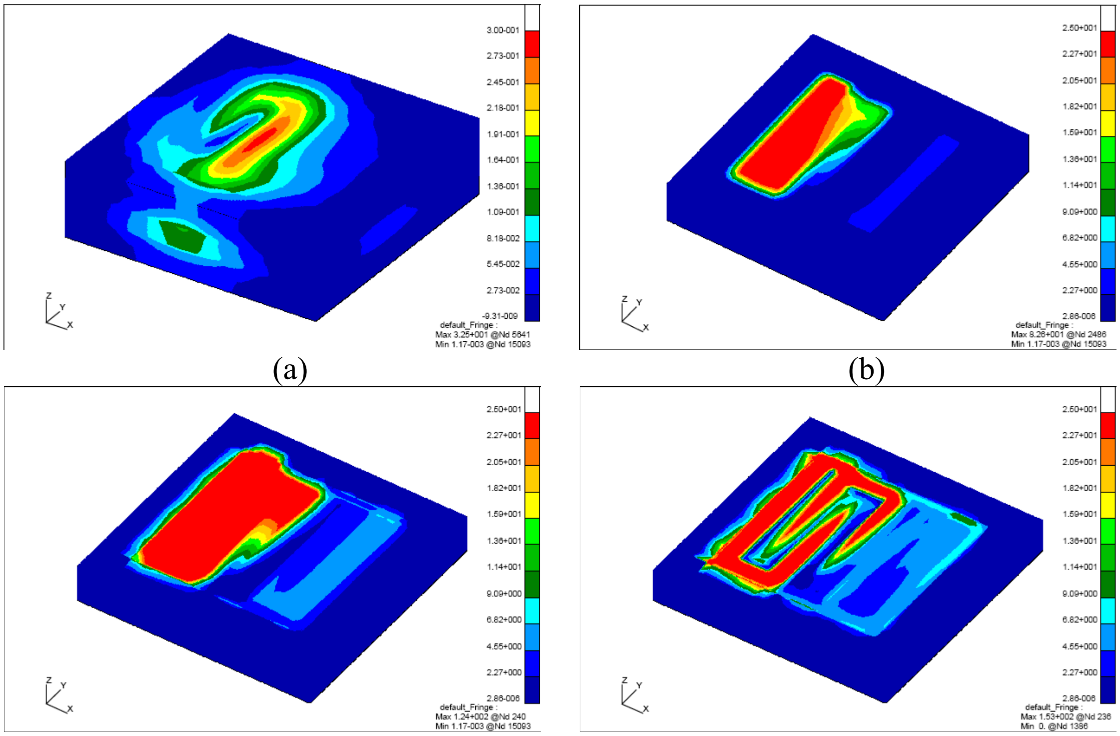

(a) (b)

(c) (d)

Figure 5.25

Near field distribution of embedded serpentine antenna, (a) top of skin (b) casing, (c) superstrate, and (d) substrate

CHAPTER VI

CONCLUSION AND FUTURE WORK

6.1 Summary

A FE-BI numerical procedure using non-stationary Krylov subspace solvers was used for designing and analyzing two miniaturize planar inverted-F antennas (PIFA), a spiral and serpentine microstrip antennas, for medical telemetry applications in the band of 402-405 MHz. The low-profile antennas were designed to match the conditions of human tissue environment as accurate as possible by using the best combination of numerical technique (FE-BI) and solver. Evaluating the characteristics of PIFA antennas in terms of return loss and radiation efficiency was accomplished. Good radiation characteristics were obtained (omni-directional, etc.) in the MICS band, as well as a good return loss and VSWR for both of the antennas when properly excited..

Based on this thesis, several observations were made and the conclusion was found that both antennas are effective radiators for the communication with medical implants. The best design can be achieved by choosing the proper substrate and superstrate material with high relative permittivity, and by varying the location of the feed point with the ground pin being in close proximity.

6.2 Future Work

The continuation of this study would be the miniaturization and dual band antenna design. The second band, which is much higher than MICS band, will be between 900 MHz and 2.45 GHz that can be used for a “wake-up” signal to conserve energy. Using higher dielectric constant for the sub- and superstrate material such as ceramic will likely to reduce the antenna size. In addition, using frequency dependent electric properties will ensure more accurate *in-silico* design.

REFERENCES

1. J. Schuster and R. Luebbers, “An FDTD algorithm for transient propagation in biological tissue with a Cole–Cole dispersion relation,” in *IEEE AP/URSI Int. Symp. Dig.*, vol. 4, June 1998, pp. 1988–1991.

2. “ETSI website.” http://www.etsi.org. European Telecommunication Standards Institute.

3. European Telecommunications Standards Institute, ETSI EN 301 839-1 Electromagnetic compatibility and Radio spectrum Matters (ERM);Radio equipment in the frequency range 402 MHz to 405 MHz for Ultra Low Power Active Medical Implants and Accessories; Part 1: Technical characteristics, including electromagnetic compatibility requirements, and test methods., 2002.

4. C. A. Balanis, Antenna Theory. John Wiley and Sons, Inc., 2nd ed., 1982.

5. J. D. Kraus, Antennas. McGraw-Hill, 1988.

6. P.-S. Kildal, Foundations of Antennas. Studentlitteratur, 2000.

7. R. C. Johnson, ed., Antenna Engineering Handbook. McGraw-Hill, Inc., 3rd ed., 1993.

8. R. W. P. King and S. G. S., Antennas in Matter. the MIT Press, 1981.

9. J. Cavuoto, “Neural engineering’s image problem,” IEEE Spectrum, Apr. 2004.

10. “Company website.” http://www.medtronic.com. Medtronic Inc.

11. R. F. Weir, P. R. Troyk, G. DeMichele, and T. Kuiken, “Implantable myoelectric sensors (IMES) for upper-extremity prosthesis control,” Engineering in Medicine and Biology Society, 2003. Proceedings of the 25th Annual International Conference of the IEEE, pp. 1562—1565, sep 2003.

12. C. Furse, “Design of an antenna for pacemaker communication,” Microwaves and RF, pp. 73—76, 2000.

13. J. Kim, and Y. Rahmat-Samii, “Implanted antennas inside a human body: simulations, designs, and characteristics,” IEEE Transactions on microwave theory and techniques, Vol. 52, No. 8, August 2004.

14. K. Gosalia, G. Lazzi, and M. Humayun, “ Investigation of a microwave data telemetry link for a retinal prosthesis,” IEEE Transactions on microwave theory and techniques, Vol. 52, No. 8, August 2004.

15. P. Soontornpipit, C. Furse, and Y. C. Chung, “Design of implantable microstrip antenna for communication with medical implants,” IEEE Transactions on microwave theory and techniques, Vol. 52, No. 8, August 2004.

16. W. Sun, G. Haubrich, and G. Dublin, “US Pat. No. 5,861,091 implantable medical device microstrip telemetry antenna,” 1999.

17. M. D. Amundson, J. A. Von Arx, W. J. Linder, P. Rawat, and W. R. Mass, “US Pat. No. 6,456,256 circumferential antenna for an implantable medical device,” 2002. USPTO.

18. J. A. Von Arx, W. R. Mass, S. T. Mazar, and M. D. Amundson, “US Pat. No. 6,708,065 antenna for an implantable pacemaker,” 2004. USPTO.

19. W. G. Scanlon, N. E. Evans, and J. B. Burns, “FDTD analysis of closed coupled 4–18 MHz radiating devices for human biotelemetry,” *Phys. Med. Biol.*, vol. 44, no. 2, pp. 335–345, 1999.

20. W. G. Scanlon, N. E. Evans, and Z. M. McCreesh, “RF performance of a 418 MHz radio telemeter packaged for human vaginal placement,” *IEEE Trans. Biomed. Eng.*, vol. 44, pp. 427–430, May 1997.

21. W. G. Scanlon, N. E. Evans, and J. B. Burns, “FDTD analysis of close-coupled 418 MHz radiating devices for human biotelemetry,” *Phys. Med. Biol.*, vol. 44, no. 2, pp. 335–345, Feb. 1999.

22. G. C. Crumley, N. E. Evans, J. B. Burns, and T. G. Trouton, “On the design and assessment of a 2.45 GHz radio telecommand system for remote patient monitoring,” *Med. Eng. Phys.*, vol. 20, no. 10, pp. 750–755, Mar. 1999.

23. R. S. Mackay, Bio-Medical Telemetry. John Wiley and Sons, Inc., 1st ed.,1968.

24. C. A. Caceres, ed., Biomedical Telemetry. Academic Press, 1965.

25. "Product catalogue." http://www.atstrack.com, 2004. Advanced Telemetry Systems, Inc.

26. C. Deffendol and C. Furse, "Microstrip antennas for dielectric property measurement," in *IEEE AP/URSI Int. Symp. Dig.*, vol. 3, Orlando, FL, July 1999, pp. 1954–1957.

27. I. J. Bahl and S. S. Stuchly, "Analysis of a microstrip covered with a lossy dielectric," *IEEE Trans. Microwave Theory Tech.*, vol. MTT-28, pp. 104–109, Feb. 1980.

28. C. M. Furse, "A meander antenna used as a human proximity sensor," Mission Res. Inc., Logan, UT, Final Rep., July 1998.

29. N. Madan, "Imbedded antennas for the measurement of electrical properties of materials," M.S. thesis, Dept. Elect. Comput. Eng., Utah State Univ., Logan, UT, 2001.

30. D. Johnson, E. Cherkaev, C. Furse, and A. Tripp, "Cross-borehole delineation of a conductive ore deposit—Experimental design," *Geophysics*, vol. 66, no. 3, pp. 824–835, 2001.

31. D. Johnson, C. Furse, and A. Tripp, "FDTD modeling and validation of EM survey tools," *Microwave Opt. Technol. Lett.*, vol. 34, no. 6, pp. 427–429, 2002.

32. P. S. Debroux, "Modeling of the electromagnetic response of geophysical targets using the (FDTD) method," *Geophys. Prospecting*, vol. 44, no. 3, pp. 457–468, 1996.

33. R. D. Nevels, D. Arndt, J. Carl, G. Raffoul, and A. Pacifico, "Microwave antenna design for myocardial tissue ablation applications," in *IEEE AP-S Int. Symp. Dig.*, vol. 3, Newport Beach, CA, June 1995, p. 1572.

34. A. S. Manolis, P. J. Wang, and N. A. Estes, "Radio frequency catheter ablation for cardiac tachyarrhythmias," *Annu. Int. Med.*, vol. 121, no. 6, pp. 452–461, Sept. 1994.

35. A. Rosen, "Microwave applications in cancer therapy, cardiology and measurement techniques:A short overview," *IEEE MTT-S Newslett.*, pp. 17–20, Fall 1990.

36. A. Guy, J. F. Lehman, and J. B. Stonebridge, "Therapeutic applications of electromagnetic power," *Proc. IEEE*, vol. 62, pp. 55–75, Jan. 1974.

37. M. F. Iskander, A. M. Tumeh, and C. M. Furse, “Evaluation and optimization of the EM characteristics of interstitial antennas for hyperthermia,” *Int. J. Radiat., Oncol., Biol., Phys.*, vol. 18, no. 4, pp. 895–902, Apr. 1990.

38. C. M. Furse and M. F. Iskander, “Three-dimensional electromagnetic power deposition in tumors using interstitial antenna arrays,” *IEEE Trans. Biomed. Eng.*, vol. 36, pp. 977–986, Oct. 1989.

39. P. C. Cherry and M. F. Iskander, “Calculations of heating patterns of an array of microwave interstitial antennas,” *IEEE Trans. Biomed. Eng.*, vol. 40, pp. 771–779, Aug. 1993.

40. J. A. Kong, Electromagnetic Wave Theory. John Wiley and Sons, 1986.

41. J. L. Volakis, A. Chatterjee, and L. Kempel, “Finite element method for electromagnetics,” *IEEE, Press*, 1993.

42. J. M. Jin, *The Finite Element Method in Electromagnetics*. New York: Wiley, 1993.

43. Stratton, J. A., *Electromagnetic Theory,* New York: McGraw-Hill, 1941.

44. L. Medgyesi-Mitschang, J. Putnam, and M. Gedera, Generalized method of moments for three-dimensional penetrable scatterers, J Opt Soc Amer A 12_1994., 1383-1398.

45. E. Yip and B. Dembart, Matrix assembly in fmm-mom codes, Tech Rep ISSTECH-97-002, Boeing Company, Seattle, WA, Jan. 1997.

46. T. K. Wu and L. L. Tsai, “Scattering from arbitrarily-shaped lossy dielectric bodies of revolution,” *Radio Sci.*, vol. 12, no. 5, pp. 709–718, 1977.

47. J. R. Mautz and R. F. Harrington, “Electromagnetic scattering from a homogeneous material body of revolution,” *Arch. Elektrotech.*, vol. 33, pp. 71–80, 1979.

48. D. E. Livesay, and K. Chen, “Electromagnetic fields induced inside arbitrarily shaped biological bodies,” *IEEE Trans. Microwave Theory Tech,* vol. MTT-22, pp. 1273-1280, December 1974.

49. J. CULLUM AND A. GREENBAUM, *Relations between Galerkin and norm minimizing iterative methods for solving linear systems*, SIAM J. Matrix Anal. Appl., 17 (1996), pp. 223–247.

50. M. EIERMANN AND O. G. ERNST, *Geometric aspects of the theory of Krylov subspace methods*, Acta Numer., 10 (2001), pp. 251–312.

51. M. HOCHBRUCK AND C. LUBICH, *Error analysis of Krylov methods in a nutshell*, SIAM J. Sci. Comput., 19 (1998), pp. 695–701.

52. Y. SAAD, *Krylov subspace methods for solving large unsymmetric linear systems*, Math. Comp., 37 (1981), pp. 105–126.

53. _____, *The Lanczos biorthogonalization algorithm and other oblique projection methods for solving large unsymmetric systems*, SIAM J. Numer. Anal., 19 (1982), pp. 485–506.

54. Y. SAAD, *Iterative methods for sparse linear systems*, Society for Industrial and Applied Mathematics, Philadelphia, PA, second ed., 2003.

55. J. Liesen and P. Tichy, ”Convergence analysis of Krylov subspace methods”,

56. Gabriel C., “Compilation of the Dielectric Properties of Body Tissue at RF and Microwave Frequencies”, Brooks Air Force Base, report no. AL/OE-TR-1996-0037, 1996.

57. Federal Communications Commission (FCC), http://www.fcc.gov/fcc-bin/dielec.sh, FCC website on Tissue Dielectrics.

58. Hurt W. D., “Radiofrequency Radiation Dosimetry Workshop”, Brooks Air Force Base, report no. AL/OE-TR-1996-0003, 1996.

59. E. Topsakal, M. Carr, J. Volakis, and M. Bleszynski, “Galerkin operators in adaptive integral method implementations,” *IEE Proc.-Microw. Antennas Propag.*, Vol. 148, No. 2, April 2001.